Auxin promotes GPI-anchored protein-mediated trafficking of ABP1 to enable cell-surface auxin signaling

Jing Wang[1,2,3], Jiang-ping Ye[1,2,3], Minmin Zhang[1], Hanqian Feng[1], Mengzhen Liu[1], Yuanzhi Huang[1,2], Tongda Xu[4], Baiyan Lu[1], Chao Li[1,2,3,*]

Affiliations:

[1]School of Life Sciences, East China Normal University, Shanghai, 200241, China.

[2]Institute of Advanced Agricultural Science and Technology, East China Normal University, Shanghai, 200241, China.

[3]Institute of Eco-Chongming, East China Normal University, Shanghai, 202162, China.

[4]Haixia Institute of Science and Technology, and College of Life Sciences, Fujian Agriculture and Forestry University, Fuzhou, Fujian 350002, China.

*Corresponding author. Email: cli@bio.ecnu.edu.cn

Present addresses:

Baiyan Lu, College of Life Science, Northwest Normal University, Lanzhou, 730070, China.

Summary

Cell-surface auxin signaling is essential for rapid cellular and growth responses to auxin. Auxin-Binding Protein 1 (ABP1) has long been proposed as an extracellular auxin receptor; however, it is predominantly retained in the endoplasmic reticulum (ER), posing a longstanding paradox. Whether ABP1 senses auxin within the ER and how the ER-retained ABP1 reaches the apoplast remain unclear. Here, we establish a dark-induced, auxin-triggered hypocotyl elongation system in *Arabidopsis,* in which *abp1* single mutants exhibit a pronounced phenotype. we show that dark-induced auxin promotes LLG1 expression and its dose-dependent interaction with ABP1, driving ABP1 trafficking from the ER to the plasma membrane (PM) through a LORELEI-like GPI-anchored protein 1 (LLG1)-based mechanism. Upon reaching the apoplast, ABP1 dissociates from LLG1 under acidic conditions, enabling activation of AHAs-mediated cell-surface signaling. Together, our results establish ABP1 as an ER-localized auxin receptor, refine the molecular framework of cell-surface auxin signaling, and uncover a GPI-AP-mediated trafficking mechanism for ER-retained receptors.

Key words: auxin receptor ABP1, dark-induced hypocotyl elongation, cell surface auxin signaling, LLG1, GPI-anchored protein

Introduction

Auxin orchestrates pleiotropic biological processes involved in plant growth and development, influencing a wide range of events from cell elongation and differentiation to organ patterning (Aryal et al., 2020; Vanneste and Friml, 2009). It has been well characterized that canonical transcriptional auxin signaling pathway relies on the TIR1/AFBs–Aux/IAAs–ARFs pathway for the regulation of auxin-responsive genes' expression (Dharmasiri et al., 2005; Kepinski and Leyser, 2005; Lavy and Estelle, 2016). Besides the transcriptional regulations occurring in nucleus, auxin also induces rapid non-transcriptional responses in apoplast within minutes, such as proton extrusion (Lin et al., 2021), membrane depolarization (Serre et al., 2021), calcium transients (Dubey et al., 2023), and cytoplasmic streaming (Kuhn et al., 2024), thereby contributing to immediate cellular and growth responses (Dubey et al., 2021; Fiedler and Friml, 2023). During the past decades, a key regulator of rapid auxin responses was isolated from maize and identified as AUXIN BINDING PROTEIN 1 (ABP1) based on its particular auxin-binding capacity (R. Hertel, 1972; Tian et al., 1995). Since then, ABP1 has been considered the best candidate for auxin receptor mediating fast auxin responses in apoplast (Eui-Jeon Woo, 2002; Löbler and Klämbt, 1985; Shoji SHIMOMURA, 1986; Xu et al., 2010). Unfortunately, the lack of obvious morphological phenotypes in *abp1* knockout mutant led to longstanding controversy over its

function (Gao et al., 2015). More recently, the function of ABP1 as an extracellular auxin receptor is confirmed, which from an auxin-sensing complex with TRANSMEMBRANE KINASE receptor-like kinases (TMKs) in an auxin-dependent manner, mediating cell wall acidification and wound-triggered vascular formation and regeneration through autoinhibited PM H^+-ATPases (AHAs) (Lin et al., 2021; Friml et al., 2022). In addition to ABP1, ABP1-like 1/2 also participate in TMKs-mediated auxin signaling and regulate developmental processes, including pavement cell interdigitation and hypocotyl elongation, indicating partially overlapping yet distinct roles of ABP1/ABLs in rapid auxin responses (Yu et al., 2023). Recent research has further demonstrated that the ABP1/ABL3–TMK1 cell-surface pathway further controls PIN2-mediated auxin fluxes required for root gravitropism (Rodriguez et al., 2025). However, no obvious phenotype has been observed in *abp1* single mutants across these systems, leaving its function enigmatic.

Paradoxically, the functional assignment of ABP1 at the cell surface contrasts with its predominant subcellular localization. ABP1 contains a C-terminal KDEL motif that confers its retention in the endoplasmic reticulum (ER), and it is confirmed that the majority of ABP1 protein resides in the ER lumen under steady-state conditions (Jones and Herman, 1993). Intriguingly, it has been found that treatment of indole-3-acetic acid (IAA) and synthetic auxin 2,4-D induces the secretion of ABP1 from ER to apoplast in *Arabidopsis* root cells and *Zea mays* BMS cells (Friml et al., 2022; Jones and Herman, 1993). Biochemically, ABP1 exhibits high binding affinity to IAA at acidic pH (15.1 ± 0.012 μM at pH 5.5), but dramatically reduced affinity at near-neutral pH (1,350 ± 150 μM at pH 7.6) (Friml et al., 2022; Tian et al., 1995). Corelating to the near-neutral pH in ER and the relatively acidic pH in apoplast, ABP1 is believed to regulate fast auxin responses in cell surface for global phosphorylation (Friml et al., 2022). Nevertheless, fundamental mechanistic questions remain unresolved: whether ABP1 senses auxin within the ER and how does auxin overcome ER retention and direct the trafficking of ABP1 from intracellular compartments to the apoplast, thereby initiating rapid cellular responses (Jones and Herman, 1993; Friml, 2022; Friml et al., 2022; Napier, 2021).

Clues to the ABP1 trafficking conundrum may lie in its interaction partners at the cell surface. Glycosylphosphatidylinositol-anchored protein (GPI-AP) represent a distinct class of secreted proteins with high transportation efficiency, which are tethered to the outer leaflet of the PM, where their high lateral mobility allows rapid redistribution and dynamic interactions with other membrane signaling components (Fujita and Kinoshita, 2012; Fujita et al., 2011; Maeda and Kinoshita, 2011; Zhang and Fujita, 2024). Plant-specific LORELEI (LRE) family GPI-APs, including LRE and LLG1/2/3, function as chaperones that direct the trafficking of CrRLK1L receptor kinases and serves as coreceptors in the RALF peptides signaling during plant development (Chao Li, 2015; Feng et al., 2019). Moreover, LLG1 has emerged as a versatile

chaperone that facilitates the immune receptor kinases LET1/2 to the PM and participate in immune responses as a coreceptor (Chen et al., 2022; Huang et al., 2020; Qiujing Shena, 2017). Recent findings also demonstrate that LLG1 participates in the auxin stimulated ROS/NO accumulation through cell surface FERONIA–RAC/ROP pathway, which stimulates the oxidation-/nitrosylation-mediated TIR1/AFB2 nuclear transport and thus transcriptional auxin responses (Lu et al., 2024). Given the specificity and high efficiency of GPI-AP secretion, it is worthwhile to investigate whether LLGs function as chaperones that mediate the trafficking of ER-retained ABP1 to the cell surface.

In this study, we establish a unique dark-induced system in which *abp1* mutant show strong phenotypes. We disclose that ER-retained ABP1 senses dark-induced auxin, interacts with LLG1 in a dose-dependent manner, and is trafficked to the cell surface via GPI-AP specific pathway. Upon reaching the PM, ABP1 dissociates from LLG1 in the acidic apoplastic environment, thereby initiating AHAs-mediated cell-surface signaling, and hypocotyl elongation. These findings identify ABP1 as an auxin receptor in the ER by revealing a GPI-AP-mediated trafficking mechanism for ER-retained receptors, thereby providing a more complete and coherent framework for fast auxin response signaling.

Results

ABP1 participates in dark-induced hypocotyl elongation

Although *ABP1* overexpression induces diverse auxin-related developmental abnormalities, the absence of clear phenotypes in *abp1* loss-of-function mutants has long impeded comprehensive understanding of *ABP1* function in auxin signaling and plant development (Gelova et al., 2021). Here, we generated the *pABP1:ABP1-eGFP* transgenic lines and found that the expression of ABP1 in the hypocotyl epidermis and cortex exhibited temporal variation, with markedly higher levels observed between days 4 to 5 (Figure S1A). Consistent with the fluorescence observations, RT-qPCR analysis further confirmed these expression patterns (Figure S1B). Notably, when we treated 4-day-old *Arabidopsis* seedlings grown under normal long-day photoperiod (16 h light/8 h dark) with darkness for 36 h, both *abp1-c1* and *abp1-TD1* mutant lines displayed significantly longer hypocotyls compared with wild type (WT) (Figure 1A). In line with this observation, growth kinetics analysis using a dual-point tracking assay (Huang et al., 2022) revealed that hypocotyl elongation proceeded through two clearly distinguishable phases: an initial fast-growing phase followed by a slower, sustained growth phase. Throughout the growth period, both *abp1* mutants exhibited significantly increased newly formed growth as well as higher rates of hypocotyl growth compared with the WT. Specifically, *abp1-c1* maintained accelerated growth throughout the entire monitoring period, whereas *abp1-TD1* displayed rapid elongation only

104 during the early phase (comparable to *abp1-c1*) followed by a gradual decline in growth rate
105 during later stages. Ultimately, both mutants developed longer hypocotyls than WT, with the
106 elongation phenotype being more pronounced in *abp1-c1* (Figure 1B). We then selected the upper
107 region of the hypocotyl as a representative zone used in all subsequent cytological analyses
108 (Figure S1C). Using this region for cell length examination, we found that under dark treatment,
109 the cortical cell area of hypocotyl was significantly larger in both *abp1* mutants compared with
110 WT (Figures 1C and S1D).

111 Next, we examined the subcellular localization of ABP1 using fluorescence intensity profile
112 and Pearson's correlation coefficient analysis. Under standard long-day photoperiod, *ABP1* signal
113 peaks showed greater colocalization with the ER marker RFP-HDEL, than with the FM4-64
114 stained PM, manifesting the predominant localization of *ABP1* in the ER (Steffens, 2011) (Figure
115 S1E). In contrast, after dark treatment for 16–18 h, majority of ABP1 fluorescent signal
116 colocalized with the PM rather than the ER marker (Figure 1D). Consistently, the Pearson's
117 correlation coefficient (r) of ABP1 signal with FM4-64 increased markedly to 0.71 after dark
118 treatment, compared to 0.46 in mock conditions, suggesting a time-dependent re-localization of
119 ABP1 from the ER to the PM (Figures S1F and S1G). Thus, this identification of the
120 ABP1-regulated hypocotyl elongation process establishes an effective system for elucidating the
121 molecular mechanisms underlying ABP1 function.

122 **Darkness induces ABP1 trafficking through auxin biosynthesis in the hypocotyl**

123 Previous study reported that darkness enhances the synthesis of auxin in cotyledon (Chen et al.,
124 2016). Therefore, we quantified the content of free IAA in the aboveground tissue of 4-day-old
125 seedling. A marked increase of IAA content was detected in the sample that exposed with 24 h
126 darkness (Figure S2A). To further explore the underlying molecular basis, we performed
127 RT-qPCR analysis of the same plant material subjected to a time-course dark treatment. As
128 anticipated, the expression of key auxin biosynthesis genes was markedly upregulated (Mano and
129 Nemoto, 2012). Specifically, the *Anthranilate Synthase Alpha1* (*ASA1)* and *Tryptophan*
130 *Aminotransferase of Arabidopsis 1* (*TAA1)* reached peak expression around 2 h, whereas *YUCCAs*
131 (*YUC3/8/9)* were strongly induced during 12–24 h (Figures 2A, 2B and S2B). Consistently, a 24 h
132 dark incubation also stimulated the expression of *pYUC9:GUS* in hypocotyl, further confirming
133 the transcriptional activation of *YUC9* (Figure S2C). In agreement with these findings, PPBo
134 (*p*-phenoxyphenyl boronic acid) (Kakei et al., 2015) significantly suppressed darkness-induced
135 hypocotyl elongation in WT seedlings. Notably, the pronounced differences observed in *abp1*
136 mutant lines under dark conditions were largely eliminated upon PPBo treatment (Figures 2C and
137 S2D). Known that the PIN family proteins-mediated polar auxin transport is essential for

138 hypocotyl cell elongation (Hu et al., 2021; Luschnig and Friml, 2024), we performed the
139 N-1-Naphthylphthalamic acid treatment (NPA, an inhibitor of PINs) (Yang et al., 2022).
140 Surprisingly, *abp1* mutants exhibited a similar level of repression as WT hypocotyls,
141 demonstrating that PINs-dependent auxin transport is strictly required for dark-induced hypocotyl
142 elongation (Figure S2E). These findings suggest that darkness promotes auxin biosynthesis and
143 thus the levels of auxin in hypocotyl, triggering ABP1-mediated hypocotyl elongation.

144 Given that the dark-induced phenotype of *abp1* is associated with increased auxin
145 biosynthesis, we asked whether it might result from altered intracellular trafficking of ABP1.
146 Upon treatment with 1 μM IAA or 10 μM NAA (naphthalene acetic acid, a synthetic auxin) for 1
147 h, the fluorescence intensity profiles of ABP1-eGFP and FM4-64 staining were well aligned, in
148 contrast to the distinct patterns observed under mock conditions (Figure 2D). Three-dimensional
149 surface plot analysis further revealed the auxin treatment-triggered a redistribution of ABP1-eGFP
150 from intracellular compartment to the PM region (Figure 2D right). In addition, the Pearson's
151 correlation coefficient between ABP1-eGFP and FM4-64 significantly increased following either
152 IAA or NAA treatment (Figures 2E and S2E). Consistently, the proportion of PM-localized
153 ABP1-eGFP in hypocotyl epidermal cells was significantly higher in auxin-treated samples
154 compared with mock treatment (Figure 2F). In line with the microscopy observations, a marked
155 reduction in ABP1 abundance was detected in the ER protein fraction of IAA-treated samples
156 compared with the mock (Figure 2G). In contrast, total ABP1 levels remained unchanged under
157 time- and concentration-dependent IAA treatment, as well as upon co-treatment with MG132, an
158 inhibitor of 26S proteasome (Figure S2F). We next examined whether auxin biosynthesis
159 influences ABP1 trafficking by analyzing its localization in both WT and the *asa1* mutant.
160 Following dark treatment, ABP1 largely remined in intracellular compartments in the *asa1* mutant,
161 in contrast to its prominent PM localization observed in WT hypocotyl cells (Figure S2G).
162 Together, these findings suggest that the darkness-induced increase in auxin levels via
163 biosynthesis drives the trafficking of ABP1 from the ER to the PM in hypocotyl cells.

164 **Dark-induced auxin-stimulates the transcriptional expression of LLG1**

165 Given the functional studies of LRE family GPI-APs as chaperones that mediate protein
166 trafficking and the involvement of LLG1 in auxin signaling, we next aimed to investigate whether
167 LRE/LLGs participate in ABP1 secretion. Between the vegetative tissue expressed LRE and
168 LLG1, LLG1 showed dramatically higher expression in hypocotyl (Figure S3A). In hypocotyl
169 epidermis and cortex of the *pLLG1:eGFP-LLG1* transgenic seedlings, the *eGFP-LLG1*
170 fluorescence peaked around day three to four, following a temporal pattern similar to *ABP1*
171 (Figure S3B). To this end, we examined the hypocotyl of *llg1-2* mutant and observed accelerated

172 hypocotyl elongation compared with WT after dark treatment (Figure 3A). Moreover, we set up a
173 local IAA application assay (dissolved in lanolin paste) to cotyledons (Bellstaedt et al., 2019) of
174 4-day-old seedlings and found that all *abp1* and *llg1* mutants displayed longer hypocotyls than
175 WT. Due to the comparable phenotype of the *abp1* mutants with *llg1*, we conducted genetic
176 crossing and obtained the double mutant. We found that the *abp1-c1 llg1-2* double mutant
177 displayed similar phenotype to that of either single mutant (Figures 3B and S3C). These results
178 suggest that ABP1 and LLG1 function cooperatively in the regulation of auxin-induced hypocotyl
179 elongation. To further investigate the auxin–*LLG1* relationship, we performed a promoter analysis
180 using PlantCARE (Lescot et al., 2002) and identified an auxin-responsive TGA-element motif in
181 the *LLG1* promoter region (Figure S3D). Notably, dark treatment significantly induced the
182 transcription of *LLG1* within 2–4 hours and the LLG1 protein also accumulated significantly
183 under dark conditions compared with the untreated controls (Figure 3C–D). Consistently, the
184 transcription of *LLG1* was significantly induced following 30 minutes of IAA treatment, and the
185 LLG1 protein was highly enriched in the PM fraction thereafter (Figures 3D and S3E). These
186 results demonstrate that dark-induced auxin promotes LLG1 expression through transcriptional
187 regulation.

188 GPI modification serves as a major sorting signal for the delivery of GPI-APs to the PM in
189 yeast, mammals, and plants (Muñiz and Riezman, 2016; Zavaliev et al., 2016). Myriocin (Myn),
190 an inhibitor of ceramide synthesis, inhibits the remodeling of GPI anchors into
191 inositolphosphoceramide (IPC)-containing forms by depleting the ceramide pool in yeast, thereby
192 impairing the transport of GPI-APs from the ER to the Golgi apparatus (Horvath et al., 1994). The
193 GPI anchors of plant GPI-APs also possess IPC tails (Xu et al., 2022), suggesting a similar
194 ceramide-dependent remodeling process to that in yeast. We then examined whether Myn could
195 disturb the function of GPI-Aps in plants. Through root hair growth observations, we found that
196 Myn treatment effectively inhibited root hair growth, phenocopying various growth-arrested
197 phenotypes of the *llg1-2* mutant (Figures S3F–G). Under Myn treatment, we observed obvious
198 intracellular retention of LLG1 in growing root hairs, indicating that inhibition of GPI-AP
199 trafficking impairs proper LLG1 localization (Figures 3E and S3H). These results suggest that, as
200 a GPI-Aps, LLG1 may utilize this trafficking pathway to mediate the targeted localization of
201 specific PM proteins. Moreover, we performed co-treatment with Myn and IAA to assess LLG1
202 subcellular localization and found that the eGFP-LLG1 signal was markedly retained within the
203 ER in hypocotyl cells (Figures 3F). Quantitative analysis of PM signal intensity showed that IAA
204 treatment increased eGFP-LLG1 accumulation at the PM, while co-treatment with Myn
205 significantly attenuated LLG1 localization to PM (Figures 3G and S3I). In addition, total protein
206 analysis by immunoblotting indicated that Myn and IAA co-treatment did not noticeably change

207 overall LLG1 abundance, indicating that Myn specifically impacts its trafficking (Figure S3J).
208 Therefore, we establish a system that enables investigation of the trafficking and function of
209 GPI-AP proteins.

210 **Auxin dose-dependently enhances the interaction between LLG1 and ABP1 in a**
211 **pH-dependent manner**

212 We carried out structural modeling of ABP1$^{\Delta SP}$ and LLG1^{core} using AlphaFold3 and identified a
213 potential strong interaction interface. Residues within this predicted binding region showed
214 pLDDT (predicted Local Distance Difference Test) scores exceeding 70, supporting the reliability
215 of the modeled interface (Figure 4A). We then examined the interaction by
216 co-immunoprecipitation (Co-IP) analysis using seedlings harboring both *pABP1:ABP1-eGFP* and
217 *pLLG1:mCherry-LLG1-Flag* transgenes and detected strong interaction between ABP1-eGFP and
218 mCherry-LLG1-Flag (Figure 4B). Moreover, luciferase-complementation assay (split-LUC) in *N.*
219 *benthamiana* leaves also demonstrated the interaction between full-length ABP1-nLuc and
220 SP-cLuc-LLG1 (Figure S4A). In particular, the ABP1$^{\Delta KDEL}$ (lacking the ER-retention KDEL motif)
221 could interact with the LLG1$^{\Delta C}$ (deficient in GPI-anchor attachment), further confirming their
222 interaction in the core regions (Figures 4C and S4B).

223 To further determine whether the distinct pH environments of the ER (~pH 7.5) and the
224 apoplast (~pH 5.5) influence the ABP1–LLG1 interaction, we performed pull-down assays across
225 a pH gradient. Interestingly, ABP1$^{\Delta SP}$ and LLG1$^{\Delta SP}$ displayed a pronounced pH-dependent
226 gradient, with strong interactions were observed at pH 7.5 and pH 8.5 and markedly weaker
227 interactions at pH5.5 (Figure 4D). These results indicated that the ABP1–LLG1 interaction is
228 preferentially stabilized under ER-like neutral pH conditions and is disfavored in the acidic
229 apoplast environment. Subsequently, we employed an IAA concentration gradient ranging from 0
230 to 2.5 μM at pH 7.5 to examine its effects on the interaction between ABP1 and LLG1. The results
231 demonstrated an auxin dose-dependent enhancement of their interaction, with stronger binding
232 observed at higher IAA concentrations (Figure 4E and S4C). However, this auxin-induced
233 enhancement was not detected at pH 5.5 (Figure S4D). Furthermore, we selected four ABP1
234 residues located at the interaction interface based on the predicted ABP1$^{\Delta SP}$–LLG1^{core}
235 structure—S106, T146, H148 and Q149—and generated alanine-substituted ABP1 variants.
236 Pull-down assays revealed that the H148A mutation markedly weakened the interaction with
237 LLG1$^{\Delta SP}$ compared with wild-type ABP1$^{\Delta SP}$ and other variants. Furthermore, based on the closer
238 spatial proximity between ABP-H148 and LLG-P113, we also tested the effect of the P113
239 mutation (P113A) and detected dramatically reduced protein interaction (Figure 4F).

240 To further investigate the function of auxin in the LLG1-mediated ABP1 transport, we

241 performed the pull-down assays using an auxin binding-pocket mutant of ABP1 (ABP1$^{M2X\Delta SP,}$
242 H59A/H61A) (Friml et al., 2022), and found that IAA failed to enhance its interaction with
243 LLG1$^{\Delta SP}$ at either pH 7.5 or pH 5.5 (Figure S4C–D). Microscopy analyses also revealed that
244 although 1 μM IAA induced the partial translocation of *ABP1^{M2X}-eGFP* to the PM, the extent of
245 this response was markedly weaker than that of wild-type ABP1 (Figure 4G). Consistent to the
246 biochemistry and microscopy results, introduction of either *ABP1^{M2X}-eGFP* or *GFP-ABP1^{M2X}*
247 under the native ABP1 promoter could not rescue the defective dark-induced hypocotyl elongation
248 phenotype of the *abp1-c1* mutant (Figure 4H). Altogether, these results indicate that auxin
249 enhances the LLG1–ABP1 interaction in a dose-dependent manner, favoring the ER over the
250 apoplast.

251 **LLG1 chaperones auxin-induced ABP1 transport through a GPI-AP trafficking pathway**

252 To investigate whether LLG1 mediates the translocation of ABP1, we co-expressed
253 *pABP1:ABP1-eGFP* with inducible *sp-mScarlet-LLG1 (XVE)* in *N. benthamiana* leaves.
254 Consistent with the results observed in seedlings, when ABP1-eGFP was expressing alone, the
255 majority remained in the ER, and this localization was not affected by *β*-estradiol treatment. In
256 contrast, IAA treatment induced significant transport to the PM (Figure S5A). Upon *β*-estradiol
257 induction of *LLG1*, a substantial proportion of ABP1-eGFP colocalized with mScarlet-LLG1 at
258 the PM, as marked by AHA2-eGFP (Figure S5B). In particular, this ABP1–LLG1 colocalization
259 was further enhanced by auxin treatment. Given that H148 is crucial for the ABP1–LLG1
260 interaction, we transiently co-expressed *pABP1:ABP1^{H148A}-eGFP* together with *sp-mScarlet-LLG1*
261 *(XVE)* in tobacco leaves and conducted fluorescence imaging. Following *β*-estradiol-induced
262 expression of mScarlet-LLG1 and auxin treatment, ABP1^{H148A}, in contrast to wild-type ABP1, was
263 retained in the ER and failed to transport to the PM (Figures 5A–B). Moreover, we crossed the
264 *pABP1:ABP1-eGFP* plants with *llg1-1* mutant and investigated the ABP1 transport. We found that
265 auxin treatment failed to promote ABP1-eGFP translocation to the PM in the absence of LLG1
266 (Figures 5C–D and S5C). These findings demonstrate that LLG1 facilitates auxin-induced ABP1
267 trafficking via protein-protein interaction.

268 Given that LLG1 traffics through a GPI-AP-specific pathway, we next asked whether ABP1
269 secretion is dependent on the GPI-anchor of LLG1. GPI is synthesized in the ER from free
270 phosphatidylinositol (PI) through a multistep process involving more than ten enzymatic reactions.
271 The mature GPI anchor is then transferred en bloc to proteins, a process mediated by GPI
272 transamidase, which cleaves the C-terminal tail and attaches the GPI moiety to the protein (Xu et
273 al., 2022). We transiently co-expressed GPI-deficient *sp-mScarlet-LLG1$^{\Delta C}$ (XVE)* with
274 *pABP1:ABP1-eGFP* in tobacco leaves and conducted fluorescence imaging. We observed that the

florescent signals of ABP1-eGFP and mScarlet-LLG1$^{\Delta C}$ appear to be colocalized in the ER. However, unlike full-length LLG1, auxin treatment failed to trigger ABP1-eGFP–mScarlet-LLG1$^{\Delta C}$ secretion to the PM (Figure 5E). Consistent with the *llg1* mutant observations, co-treatment with GPI-AP trafficking inhibitor Myn also suppressed the effect of IAA treatment to promote the ABP1-eGFP secretion to the PM, and gave rise to some punctate structures reminiscent of the puncta of misfolded GPI-APs resulted from chemical-induced ER stress (Satpute-Krishnan et al., 2014) (Figure 5F and S5D–E). These results suggest that LLG1 relies on its GPI-anchor to facilitate the transportation of ABP1. In these observations, we noted that auxin-induced PM accumulation of ABP1 requires around half an hour. This timescale aligns with the phenotypic manifestation in *abp1* mutants, in which significant differences in hypocotyl elongation rates appear after 2.5 h of dark treatment. A similar pattern has been reported in roots, where PM-proximal aggregation of ABP1 is typically detected around 3 h after IAA treatment (Friml et al., 2022). We consider this kinetics reasonable, given that the *de novo* LLG1 synthesis and subsequent GPI-AP-dependent trafficking both play essential roles in ABP1 secretion.

ABP1 regulates AHAs-mediated apoplast acidification in dark-induced hypocotyl elongation

To further investigate the interaction between ABP1 and LLG1, we performed Förster resonance energy transfer-fluorescence lifetime imaging microscopy (FRET-FLIM) analysis. The donor-acceptor pair ABP1-mTurquoise2–LLG1-mVenus was transiently expressed in tobacco leaves. We observed that the co-expression of LLG1-mVenus marked reduced the fluorescence lifetime of ABP1-mTurquoise2 at both the ER and the PM. Notably, the FRET efficiency of the ABP1–LLG1 interaction was significantly higher in the ER (~60–80%) than at the PM (~40–60%) (Figure 6A). Moreover, given that ABP1 collaborates with TMKs to regulate cell wall acidification through autoinhibited PM H^+-ATPases 1/2 (AHA1/2) (Lin et al., 2021; Friml et al., 2022), we examined the phenotypes of *aha1/2* mutants in our established dark-growth system. Both *aha1-7* and *aha2-4* mutants displayed shorter hypocotyl whereas a constitutively active AHA1 mutant, *ost2-2D* exhibited longer hypocotyl compared with WT (Figures S6A). Under IAA treatment, *aha2-4* and *ost2-2D* exhibited phenotypes resembling those observed under dark conditions, though *aha1-7* showed no significant difference from WT (Figure S6B). We further focused on AHA2 and generated the *abp1-c1 aha2-4* double mutant. This double mutant displayed dark-induced shorter hypocotyl similar to *aha2-4* (Figures 6C and S6C). These results linked the ABP1 to downstream AHA2 in the dark-promoted hypocotyl elongation.

We next applied the membrane-impermeable pH indicator HPTS (8-hydroxypyrene-1,3,6-trisulfonic acid trisodium salt) (Amali et al., 2011; Liu et al., 2025) and observed that dark treatment significantly reduced the apoplast pH in the hypocotyl epidermis and

309 cortex (Figure S7A). Based on that, we further examined the apoplast pH in *abp1-c1* under dark
310 conditions and discovered that the *abp1* apoplast was more acidic than that in the WT. Moreover,
311 additional auxin treatment induced a rapid and pronounced acidification in WT apoplast; by
312 contrast, the *abp1-c1* mutant failed to respond to auxin treatment (Figures 6D and S7B). Also, the
313 pH measured by the HPTS-pH calibration consistent with this finding (Figure S7C–D).
314 Nevertheless, no obvious differences were detected between WT and *abp1-c1* under light-grown
315 conditions regarding auxin responses (Figure S7E). The phosphorylation of Thr947 in AHA2 acts
316 as a molecular switch controlling proton pump activity to induced H^+ efflux[6,43,44]. When we
317 applied IAA treatment under dark conditions, it rapidly increased the phosphorylation levels of
318 AHA2 Thr947 in WT seedlings but not in the *abp1-c1* mutant (Figure 6E). Since the Thr881 has
319 also been reported an activation site for the regulation of AHA2proton pump activity (Fuglsang et
320 al., 2014; Lin et al., 2021), we introduced the *pAHA2:AHA2*$^{T881A/T947A}$ construct to the *aha2-4*
321 background and found that this variant failed to rescue the dark-induced defective hypocotyl
322 growth of *aha2-4* (Figure 6F). In addition, we applied Myn pretreatment before the treatment of
323 dark and auxin for the investigation of LLG1 participation. Notably, the Myn application
324 significantly disturbed the auxin-induced apoplast acidification in hypocotyl (Figures 6G and S7F).
325 Furthermore, we also examined the Thr947 phosphorylation status in the *llg1-2* mutant. Upon
326 auxin treatment under dark conditions, however, this auxin-induced phosphorylation response was
327 absent in *llg1-2*, mimicking the phenomenon observed in *abp1* mutant (Figure 6H). These results
328 together establish a causal linkage between LLG1-facilitated ABP1 transport and AHA2-mediated
329 apoplast acidification.

330 **Discussion**

331 Cell surface-mediated auxin signaling has long been recognized; however, the functional
332 characterization of ABP1 as an auxin receptor remains largely unresolved. In particular, the
333 mechanism by which auxin regulates the secretion of this ER-retained receptor to the apoplast,
334 thereby initiating cell surface auxin signaling, has remained a mystery (Jones and Herman, 1993;
335 Friml, 2022; Friml et al., 2022; Napier, 2021). In this study, by capture the critical expression
336 peak of ABP1, we established an endogenous auxin induction system in which 4-day-old
337 seedlings were subjected to 16–36 h of darkness, and observed pronounced hypocotyl
338 elongation defects in *abp1* mutants. We found that this darkness induction system stimulates
339 auxin synthesis and consequently upregulates LLG1 expression in hypocotyl cells. Using this
340 system, we reveal that auxin dose-dependently promotes the interaction between LLG1 and
341 ABP1 and facilitates their vesicular trafficking via a unique GPI-AP pathway. Upon reaching
342 the outer leaflet of the PM, ABP1 dissociates from LLG1 due to the acidic apoplastic pH and

343 subsequently coordinates with AHAs pathway for the regulation of hypocotyl elongation
344 (Figure 7).

345 Our study establishes ABP1 as a bona fide functional auxin receptor. Importantly, we show
346 that ABP1 exhibits IAA dose-dependent interaction with LLG1 at neutral ER pH conditions. This
347 raises the question of how auxin functions in this process. In this study, our results show that IAA
348 treatment enhances the ABP1-LLG1 interaction in a dose-dependent manner at neutral ER pH
349 conditions, illustrating that ABP1 is capable of sensing auxin within the ER. In this context, LLG1
350 acts as a co-factor that enables this interaction, thereby challenging the prevailing view that ABP1
351 is unable to bind auxin in the ER (Friml et al., 2022). Moreover, loss of auxin-binding capability
352 in $ABP1^{M2X,}$ as well as disruption of LLG1, both lead to defects in dark/auxin-induced ABP1
353 transport and hypocotyl elongation. These studies demonstrate that auxin and LLG1 enable ABP1
354 to transition from an intracellular sensing state to an active signaling state at the cell surface.
355 Furthermore, previous structural analyses of ABP1 showed no major global conformational
356 rearrangements upon auxin binding in crystal structures (Dahlke et al., 2009; Eui-Jeon Woo, 2002).
357 Using Chai-1 molecule docking analysis, we found that, in addition to binding to the canonical
358 pocket of ABP1, IAA could insert into the LLG1 protein. In certain working models, the predicted
359 IAA binding sites locate close to the ABP1–LLG1 interaction interface (Figure S7H). This
360 structural prediction provides a potential mechanistic explanation for how auxin regulate this
361 process. Altogether, these findings establish a direct functional basis for ABP1 as an auxin
362 receptor and indicate that auxin perception can be initiated within the ER.

363 A central finding of this study is that the GPI-AP LLG1 promotes ABP1 secretion via a
364 specialized GPI-AP trafficking pathway. In flowering plants, the C-terminal KDEL motif of ABP1
365 normally mediates its retrieval from the Golgi to the ER, thereby limiting its secretion (Jones and
366 Herman, 1993). Our results indicate that auxin enables LLG1 to overcome this retention,
367 facilitating the delivery of ABP1 to the apoplast where it can function in auxin perception and
368 signaling. Several mechanisms regarding to the release of ER-resident KDEL-bearing proteins
369 have been hypothesized (Palazzo et al., 2022). Here we reveal the mechanism that auxin enables
370 LLG1 to bypass the ER retention appears to happen through saturation of the KDEL receptor
371 retrieval machinery caused by high LLG1 expression driving the ER exit of large amounts of
372 ABP1, ultimately facilitating the delivery of ABP1 to the apoplast, where it participates in auxin
373 perception and signaling. This mode of transport is distinct from conventional vesicular trafficking
374 used by most membrane and secretory proteins and is characteristic of GPI-APs, which are sorted
375 through sphingolipid-dependent membrane microdomains (Guillaume Alain Castillon, 2013).
376 Such lipid-based sorting is thought to enhance trafficking efficiency and is conserved across
377 eukaryotes (Zhang and Fujita, 2024). In addition, GPI-APs are tethered to the outer leaflet of the

PM, conferring high lateral mobility that supports rapid redistribution during signaling events (Zhang and Fujita, 2024). Consistent with these properties, LLG1 may also contribute to the lateral organization of ABP1 at the PM, thereby facilitating its interaction with TMK1/4 receptor kinases and promoting downstream AHA1/2-mediated auxin signaling.

This study reveals that the interaction between LLG1 and ABP1 is regulated by pH, being strong under the near-neutral conditions of the ER but markedly weaker in the more acidic apoplastic environment. We found that auxin binding to ABP1 modulates its interaction with LLG1 in a manner that stabilizes the ABP1–LLG1 complex under neutral pH conditions. Upon secretion into the apoplast, the decrease in pH is expected to alter electrostatic interactions and local protein conformation, thereby weakening ABP1–LLG1 association and favoring a transition from ER-localized complex formation to interactions between ABP1 and TMK1/4 receptor kinases. We identified $ABP1^{H148}$ as a critical site for LLG1 interaction. The histidine residue can be reversible protonated under different pH conditions, leading to changes in hydrogen bond formation. Therefore, modification of H148 likely underlies the pH-dependent variation in ABP1–LLG1 binding affinity. Notably, this residue is essential for ABP1 trafficking to the apoplast, indicating that its membrane translocation is mechanistically coupled to LLG1 interaction. This pH-dependent modulation of protein-protein interactions provides a plausible mechanism by which ABP1 transitions from a trafficking-associated state to a signaling-competent state at the cell surface. Notably, while LLG1 has been well characterized as a co-receptor of FER that mediates RALF peptide perception and subsequent extracellular alkalinization (Haruta et al., 2014; Xiao et al., 2019), this study uncovers its novel function in ABP1 trafficking. This finding reveals a novel functional divergence for LLG1, demonstrating its capacity to operate autonomously from the canonical FER signaling pathway.

References

Amali, A.J., Awwad, N.H., Rana, R.K., and Patra, D. (2011). Nanoparticle assembled microcapsules for application as pH and ammonia sensor. Anal. Chim. Acta *708*, 75-83. https://doi.org/10.1016/j.aca.2011.10.001.

Aryal, B., Jonsson, K., Baral, A., Sancho-Andres, G., Routier-Kierzkowska, A. L., Kierzkowski, D., and Bhalerao, R. P. (2020). Interplay between Cell Wall and Auxin Mediates the Control of Differential Cell Elongation during Apical Hook Development. Curr. Biol. *30*, 1733-1739. https://doi.org/10.1016/j.cub.2020.02.055.

Bellstaedt, J., Trenner, J., Lippmann, R., Poeschl, Y., Zhang, X., Friml, J., Quint, M., and Delker, C. (2019). A Mobile Auxin Signal Connects Temperature Sensing in Cotyledons with Growth Responses in Hypocotyls. Plant Physiol. *180*, 757-766. https://doi.org/10.1104/pp.18.01377.

Li, C., Yeh, F. L., Cheung, A. Y., Duan, Q., Kita, D., Liu, M. C., Maman, J., Luu, E. J., Wu, B. W., Gates, L., et al. (2015). Glycosylphosphatidylinositol-anchored proteins as chaperones and co-receptors for FERONIA receptor kinase signaling in Arabidopsis. eLife *4*, e06587.

415 https://doi.org/10.7554/eLife.06587.

416 Chen, L., Tong, J., Xiao, L., Ruan, Y., Liu, J., Zeng, M., Huang, H., Wang, J.W., and Xu, L. (2016).
417 YUCCA-mediated auxin biogenesis is required for cell fate transition occurring during de novo root
418 organogenesis in Arabidopsis. J. Exp. Bot. *67*, 4273-4284. https://doi.org/10.1093/jxb/erw213.

419 Chen, R., Sun, P., Zhong, G., Wang, W., and Tang, D. (2022). The RECEPTOR-LIKE PROTEIN53
420 immune complex associates with LLG1 to positively regulate plant immunity. J. Integr. Plant Biol. 64,
421 1833-1846. https://doi.org/10.1111/jipb.13327.

422 Dahlke, R.I., Luthen, H., and Steffens, B. (2009). The auxin-binding pocket of auxin-binding protein 1
423 comprises the highly conserved boxes a and c. Planta *230*, 917-924.
424 https://doi.org/10.1007/s00425-009-0995-2.

425 Dharmasiri, N., Dharmasiri, S., and Estelle, M. (2005). The F-box protein TIR1 is an auxin receptor.
426 Nature *435*, 441-445. https://doi.org/10.1038/nature03542.

427 Dubey, S.M., Han, S., Stutzman, N., Prigge, M.J., Medvecka, E., Platre, M.P., Busch, W., Fendrych,
428 M., and Estelle, M. (2023). The AFB1 auxin receptor controls the cytoplasmic auxin response pathway
429 in Arabidopsis thaliana. Mol. Plant *16*, 1120-1130. https://doi.org/10.1016/j.molp.2023.06.008.

430 Dubey, S.M., Serre, N.B.C., Oulehlová, D., Vittal, P., and Fendrych, M. (2021). No Time for
431 Transcription—Rapid Auxin Responses in Plants. Cold Spring Harb. Perspect. Biol. *13*, a039891.
432 https://doi.org/10.1101/cshperspect.a039891.

433 Eui-Jeon Woo, J.M., James Bauly, Jin-Gui Chen, Michael Venis, Richard M.Napier and Richard
434 W.Pickersgill (2002). Crystal structure of auxin-binding protein 1 in complex with auxin. EMBO J. *21*,
435 2877-2885. https://doi.org/10.1093/emboj/cdf291.

436 Feng, H., Liu, C., Fu, R., Zhang, M., Li, H., Shen, L., Wei, Q., Sun, X., Xu, L., Ni, B., *et al.* (2019).
437 LORELEI-LIKE GPI-ANCHORED PROTEINS 2/3 Regulate Pollen Tube Growth as Chaperones and
438 Coreceptors for ANXUR/BUPS Receptor Kinases in Arabidopsis. Mol. Plant *12*, 1612-1623.
439 https://doi.org/10.1016/j.molp.2019.09.004.

440 Fiedler, L. and Friml, J. (2023). Rapid auxin signaling: Unknowns old and new. Curr. Opin. Plant Biol.
441 *75*, 102443. https://doi.org/10.1016/j.pbi.2023.102443.

442 Friml, J. (2022). Fourteen Stations of Auxin. Cold Spring Harb. Perspect. Biol. *14*, a039859.
443 https://doi.org/10.1101/cshperspect.a039859.

444 Friml, J., Gallei, M., Gelová, Z., Johnson, A., Mazur, E., Monzer, A., Rodriguez, L., Roosjen, M.,
445 Verstraeten, I., Živanović, B. D., et al. (2022). ABP1-TMK auxin perception for global
446 phosphorylation and auxin canalization. Nature *609*, 575-581.
447 https://doi.org/10.1038/s41586-022-05187-x.

448 Fuglsang, A.T., Kristensen, A., Cuin, T.A., Schulze, W.X., Persson, J., Thuesen, K.H., Ytting, C.K.,
449 Oehlenschlaeger, C.B., Mahmood, K., Sondergaard, T.E., et al. (2014). Receptor kinase-mediated
450 control of primary active proton pumping at the plasma membrane. Plant J. *80*, 951-964.
451 https://doi.org/10.1111/tpj.12680.

452 Fujita, M. and Kinoshita, T. (2012). GPI-anchor remodeling: potential functions of GPI-anchors in
453 intracellular trafficking and membrane dynamics. Biochim. Biophys. Acta *1821*, 1050-1058.
454 https://doi.org/10.1016/j.bbalip.2012.01.004.

455 Fujita, M., Watanabe, R., Jaensch, N., Romanova-Michaelides, M., Satoh, T., Kato, M., Riezman, H.,
456 Yamaguchi, Y., Maeda, Y., and Kinoshita, T. (2011). Sorting of GPI-anchored proteins into ER exit

sites by p24 proteins is dependent on remodeled GPI. J. Cell Biol. *194*, 61-75. https://doi.org/10.1083/jcb.201012074.

Gao, Y., Zhang, Y., Zhang, D., Dai, X., Estelle, M., and Zhao, Y. (2015). Auxin binding protein 1 (ABP1) is not required for either auxin signaling or Arabidopsis development. Proc. Natl. Acad. Sci. U.S.A. *112*, 2275-2280. https://doi.org/10.1073/pnas.1500365112.

Gelová, Z., Gallei, M., Pernisová, M., Brunoud, G., Zhang, X., Glanc, M., Li, L., Michalko, J., Pavlovičová, Z., Verstraeten, I., et al. (2021). Developmental roles of Auxin Binding Protein 1 in Arabidopsis thaliana. Plant Sci. *303*, 110750. https://doi.org/10.1016/j.plantsci.2020.110750.

Guillaume Alain Castillon, L.M., and Reika Watanabe (2013). Apical sorting of lysoGPI-anchored proteins occurs independent of association with detergent-resistant membranes but dependent on their N-glycosylation. Molecular Biology of the Cell *24*, 2021-2033. https://doi.org/10.1091/mbc.E13-03-0160.

Haruta, M., Sabat, G., Stecker, K., Minkoff, B. B. and Sussman, M. R. (2014). A peptide hormone and its receptor protein kinase regulate plant cell expansion. Science *343*, 408-411. https://doi.org/10.1126/science.1244454.

Horvath, A., Sutterlin, C., Manning-Krieg, U., Movva, N. R. and Riezman, H. (1994). Ceramide synthesis enhances transport of GPI-anchored proteins to the Golgi apparatus in yeast. EMBO J. *13*, 3687-3695. https://doi.org/10.1002/j.1460-2075.1994.tb06678.x.

Hu, T., Yin, S., Sun, J., Linghu, Y., Ma, J., Pan, J., and Wang, C. (2021). Clathrin light chains regulate hypocotyl elongation by affecting the polarization of the auxin transporter PIN3 in Arabidopsis. J. Integr. Plant Biol. *63*, 1922-1936. https://doi.org/10.1111/jipb.13171.

Huang, S., Yang, C. and Li, L. (2022). Unraveling the Dynamic Integration of Auxin, Brassinosteroid and Gibberellin in Early Shade-Induced Hypocotyl Elongation. Phenomics *2*, 119-129. https://doi.org/10.1007/s43657-022-00044-3.

Huang, Y., Yin, C., Liu, J., Feng, B., Ge, D., Kong, L., Ortiz-Morea, F. A., Richter, J., Hauser, M. T., Wang, W. M., et al. (2020). A trimeric CrRLK1L-LLG1 complex genetically modulates SUMM2-mediated autoimmunity. Nat. Commun. *11*, 4859. https://doi.org/10.1038/s41467-020-18600-8.

Jones, A. M. and Herman, E. M. (1993). KDEL-Containing Auxin-Binding Protein Is Secreted to the Plasma Membrane and Cell Wall. Plant Physiol. *101*, 595-606. https://doi.org/10.1104/pp.101.2.595.

Kakei, Y., Yamazaki, C., Suzuki, M., Nakamura, A., Sato, A., Ishida, Y., Kikuchi, R., Higashi, S., Kokudo, Y., Ishii, T., et al. (2015). Small-molecule auxin inhibitors that target YUCCA are powerful tools for studying auxin function. Plant J. *84*, 827-837. https://doi.org/10.1111/tpj.13032.

Kepinski, S., and Leyser, O. (2005). The Arabidopsis F-box protein TIR1 is an auxin receptor. Nature *435*, 446-451. https://doi.org/10.1038/nature03542.

Kuhn, A., Roosjen, M., Mutte, S., Dubey, S.M., Carrillo Carrasco, V.P., Boeren, S., Monzer, A., Koehorst, J., Kohchi, T., Nishihama, R., et al. (2024). RAF-like protein kinases mediate a deeply conserved, rapid auxin response. Cell *187*, 130-148. https://doi.org/10.1016/j.cell.2023.11.021.

Lavy, M. and Estelle, M. (2016). Mechanisms of auxin signaling. Development *143*, 3226-3229. https://doi.org/10.1242/dev.131870.

Lescot, M., Déhais, P., Thijs, G., Marchal, K., Moreau, Y., Van de Peer, Y., Rouzé, P., and Rombauts, S. (2002). PlantCARE, a database of plant cis-acting regulatory elements and a portal to tools for in

499 silico analysis of promoter sequences. Nucleic Acids Res. *30*, 325-327.
500 https://doi.org/10.1093/nar/30.1.325.

501 Lin, W., Zhou, X., Tang, W., Takahashi, K., Pan, X., Dai, J., Ren, H., Zhu, X., Pan, S., Zheng, H., et al.
502 (2021). TMK-based cell-surface auxin signalling activates cell-wall acidification. Nature *599*, 278-282.
503 https://doi.org/10.1038/s41586-021-03976-4.

504 Liu, Z., Chu, X., Ren, W., Cheng, L., Liu, C., Wang, C., Gao, S., Dai, S., and Li, C. (2025). PCP-B
505 peptides and CrRLK1L receptor kinases control pollination via pH gating of aquaporins in Arabidopsis.
506 Dev. Cell *60*, 1336-1347. https://doi.org/10.1016/j.devcel.2024.12.026.

507 Löbler, M. and Klämbt, D. (1985). Auxin-binding protein from coleoptile membranes of corn (Zea
508 mays L.). I. Purification by immunological methods and characterization. J. Biol. Chem. *260*,
509 9848-9853. https://doi.org/10.1016/s0021-9258(17)39314-6.

510 Lu, B., Wang, S., Feng, H., Wang, J., Zhang, K., Li, Y., Wu, P., Zhang, M., Xia, Y., Peng, C., et al.
511 (2024). FERONIA-mediated TIR1/AFB2 oxidation stimulates auxin signaling in Arabidopsis. Mol.
512 Plant *17*, 772-787. https://doi.org/10.1016/j.molp.2024.04.002.

513 Luschnig, C., and Friml, J. (2024). Over 25 years of decrypting PIN-mediated plant development. Nat.
514 Commun. *15*, 9904. https://doi.org/10.1038/s41467-024-54240-y.

515 Maeda, Y. and Kinoshita, T. (2011). Structural remodeling, trafficking and functions of
516 glycosylphosphatidylinositol-anchored proteins. Prog. Lipid Res. *50*, 411-424.
517 https://doi.org/10.1016/j.plipres.2011.05.002.

518 Mano, Y. and Nemoto, K. (2012). The pathway of auxin biosynthesis in plants. J. Exp. Bot. *63*,
519 2853-2872. https://doi.org/10.1093/jxb/ers091.

520 Muñiz, M. and Riezman, H. (2016). Trafficking of glycosylphosphatidylinositol anchored proteins
521 from the endoplasmic reticulum to the cell surface. J. Lipid Res. *57*, 352-360.
522 https://doi.org/10.1194/jlr.R062760.

523 Napier, R. (2021). The Story of Auxin-Binding Protein 1 (ABP1). Cold Spring Harb. Perspect. Biol. *13*,
524 a039909. https://doi.org/10.1101/cshperspect.a039909.

525 Palazzo, F. C., Sitia, R. and Tempio, T. (2022). Selective Secretion of KDEL-Bearing Proteins:
526 Mechanisms and Functions. Front. Cell Dev. Biol. *10*, 967875.
527 https://doi.org/10.3389/fcell.2022.967875.

528 Qiujing Shena, G. B., Huairong Pan, Silke Robatzek, and Dingzhong Tang (2017). Arabidopsis
529 glycosylphosphatidylinositol-anchored protein LLG1 associates with and modulates FLS2 to regulate
530 innate immunity. Proc. Natl. Acad. Sci. U.S.A. *114*, 5749-5754.
531 https://doi.org/10.1073/pnas.1614468114.

532 R. Hertel, K.-S. T., and V. E. A. Russo (1972). In-vitro Auxin Binding to Particulate Cell Fractions
533 from Corn Coleoptiles. Planta *107*, 325-340. https://doi.org/10.1007/BF00386394.

534 Rodriguez, L., Fiedler, L., Zou, M., Giannini, C., Monzer, A., Vladimirtsev, D., Randuch, M., Yu, Y.,
535 Gelová, Z., Verstraeten, I., et al. (2025). ABP1/ABL3-TMK1 cell-surface auxin signaling targets
536 PIN2-mediated auxin fluxes for root gravitropism. Cell *188*, 6138-6150.
537 https://doi.org/10.1016/j.cell.2025.08.026.

538 Satpute-Krishnan, P., Ajinkya, M., Bhat, S., Itakura, E., Hegde, Ramanujan S., and
539 Lippincott-Schwartz, J. (2014). ER Stress-Induced Clearance of Misfolded GPI-Anchored Proteins via
540 the Secretory Pathway. Cell *158*, 522-533. https://doi.org/10.1016/j.cell.2014.06.026.

Serre, N.B.C., Kralik, D., Yun, P., Slouka, Z., Shabala, S., and Fendrych, M. (2021). AFB1 controls rapid auxin signalling through membrane depolarization in Arabidopsis thaliana root. Nat. Plants *7*, 1229-1238. https://doi.org/10.1038/s414.

Shimomura, S. (2006). Identification of a glycosylphosphatidylinositol-anchored plasma membrane protein interacting with the C-terminus of auxin-binding protein 1: a photoaffinity crosslinking study. Plant Mol. Biol. *60*, 663-677. https://doi.org/10.1007/s11103-005-5471-1.

Shoji SHIMOMURA, T.S.F., and Toshio FUKUI (1986). Purifcation and Properties of an Auxin-Binding Proteinfrom Maize Shoot Membranes. J. Biochem. *99*, 1513-1524. https://doi.org/10.1093/oxfordjournals.jbchem.a135621.

Klode, M., Dahlke, R. I., Sauter, M., and Steffens, B. (2011). Expression and Subcellular Localization of Arabidopsis thaliana Auxin-Binding Protein 1 (ABP1). J. Plant Growth Regul. *30*, 416-424. https://doi.org/10.1007/s00344-011-9203-2.

Tian, H., Klämbt, D., and Jones, A.M. (1995). Auxin-binding Protein 1 Does Not Bind Auxin within the Endoplasmic Reticulum Despite This Being the Predominant Subcellular Location for This Hormone Receptor. J. Biol. Chem. *270*, 26962-26969. https://doi.org/10.1074/jbc.270.45.26962.

Vanneste, S., and Friml, J. (2009). Auxin: a trigger for change in plant development. Cell *136*, 1005-1016. https://doi.org/10.1016/j.cell.2009.03.001.

Xiao, Y., Stegmann, M., Han, Z., DeFalco, T.A., Parys, K., Xu, L., Belkhadir, Y., Zipfel, C., and Chai, J. (2019). Mechanisms of RALF peptide perception by a heterotypic receptor complex. Nature *572*, 270-274. https://doi.org/10.1038/s41586-019-1409-7.

Xu, T., Wen, M., Nagawa, S., Fu, Y., Chen, J.G., Wu, M.J., Perrot-Rechenmann, C., Friml, J., Jones, A.M., and Yang, Z. (2010). Cell surface- and rho GTPase-based auxin signaling controls cellular interdigitation in Arabidopsis. Cell *143*, 99-110. https://doi.org/10.1016/j.cell.2010.09.003.

Xu, Z., Gao, Y., Gao, C., Mei, J., Wang, S., Ma, J., Yang, H., Cao, S., Wang, Y., Zhang, F.*, et al.* (2022). Glycosylphosphatidylinositol anchor lipid remodeling directs proteins to the plasma membrane and governs cell wall mechanics. Plant Cell *34*, 4778-4794. https://doi.org/10.1093/plcell/koac257.

Yang, Z., Xia, J., Hong, J., Zhang, C., Wei, H., Ying, W., Sun, C., Sun, L., Mao, Y., Gao, Y.*,* et al. (2022). Structural insights into auxin recognition and efflux by Arabidopsis PIN1. Nature *609*, 611-615. https://doi.org/10.1038/s41586-022-05143-9.

Yu, Y., Tang, W., Lin, W., Li, W., Zhou, X., Li, Y., Chen, R., Zheng, R., Qin, G., Cao, W.*,* et al. (2023). ABLs and TMKs are co-receptors for extracellular auxin. Cell *186*, 5457-5471. https://doi.org/10.1016/j.cell.2023.10.017.

Zavaliev, R., Dong, X., and Epel, B.L. (2016). Glycosylphosphatidylinositol (GPI) modification serves as a primary plasmodesmal targeting signal. Plant physiol. *172*, 1061-1073. https://doi.org/10.1104/pp.16.01026.

Zhang, Q., and Fujita, M. (2024). Why nature evolved GPI-anchored proteins: unique structure characteristics enable versatile cell surface functions. Glycobiology *34*, cwae089. https://doi.org/10.1093/glycob/cwae089.

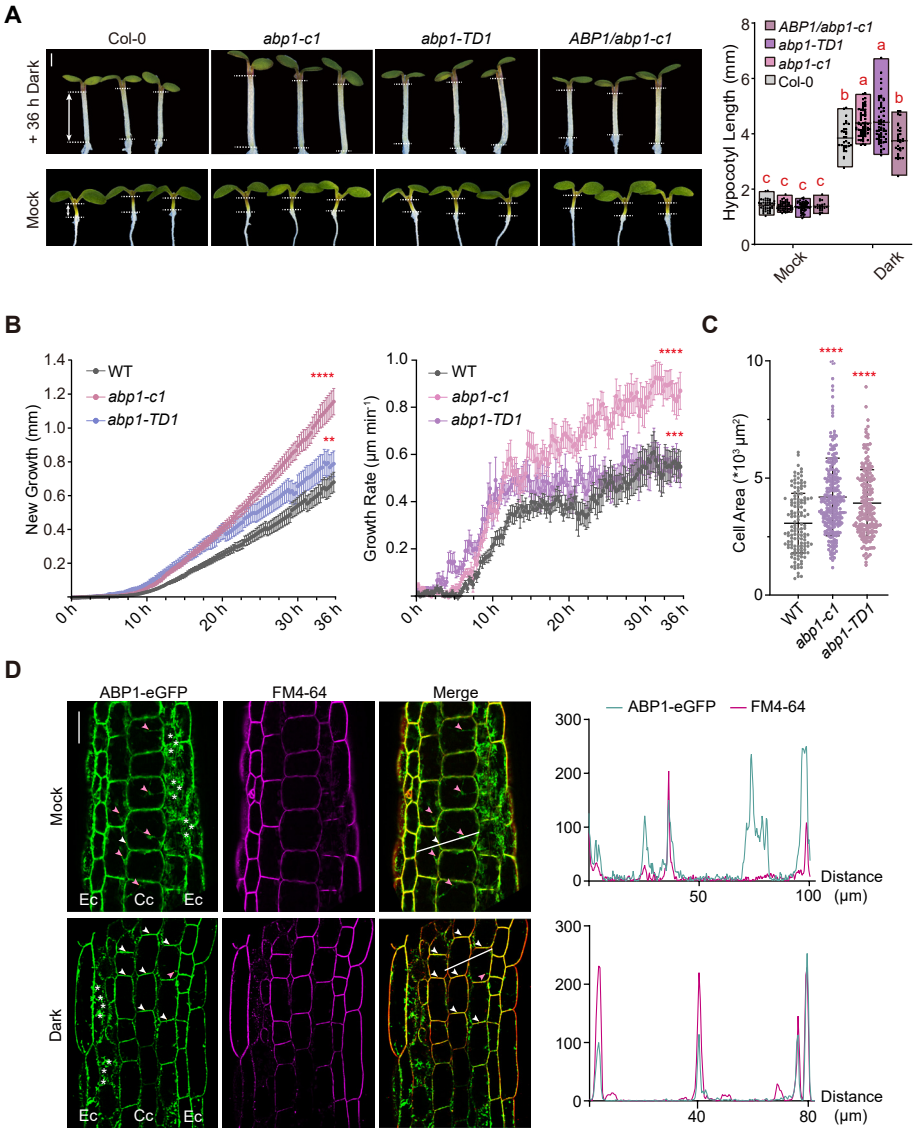

Figure 1. ABP1 participates in dark-induced hypocotyl elongation in *Arabidopsis*

(A) Phenotype analysis and quantification of hypocotyl length in 4-day-old *abp1-c1*, *abp1-TD1 and pABP1:ABP1-eGFP/abp1-c1* seedlings subjected to mock or dark treatment for 36 h. $n \geq 21$ hypocotyls. Scale bar, 2 mm.

(B) Time-lapse analysis of hypocotyl new growth and growth rate in 4-day-old WT, *abp1-c1* and *abp1-TD1* seedlings during continuous dark treatment for 36 h. Images were captured every 15 min. $n \geq 28$ hypocotyls.

(C) Quantification of hypocotyl cell areas in 4-day-old WT, *abp1-c1* and *abp1-TD1* seedlings subjected to dark treatment for 36 h. $n \geq 135$ cells from 24–39 hypocotyls.

(D) Confocal microscopy imaging and fluorescence plot profiling of ABP1-eGFP in hypocotyl cortical cells of seedlings subjected to dark treatment for 18 h. Ec, epidermal cell; Cc, cortex cell. stars lable the unfocused areas. White line is used for fluorescence intensity measurement; FM4-64 labels the PM; white arrowheads indicate the colocalized signal; pink arrowheads indicate the non-colocalized signal; Scale bar, 50 μm.

In (A–C), data are presented as mean ± SD. Significant differences were determined using two-way ANOVA. Different lowercase letters indicate significant differences at $P < 0.05$ (A). Significant differences were determined using Student's *t*-test (B–C). $^{**}P < 0.01$, $^{***}P < 0.001$, $^{****}P < 0.0001$.

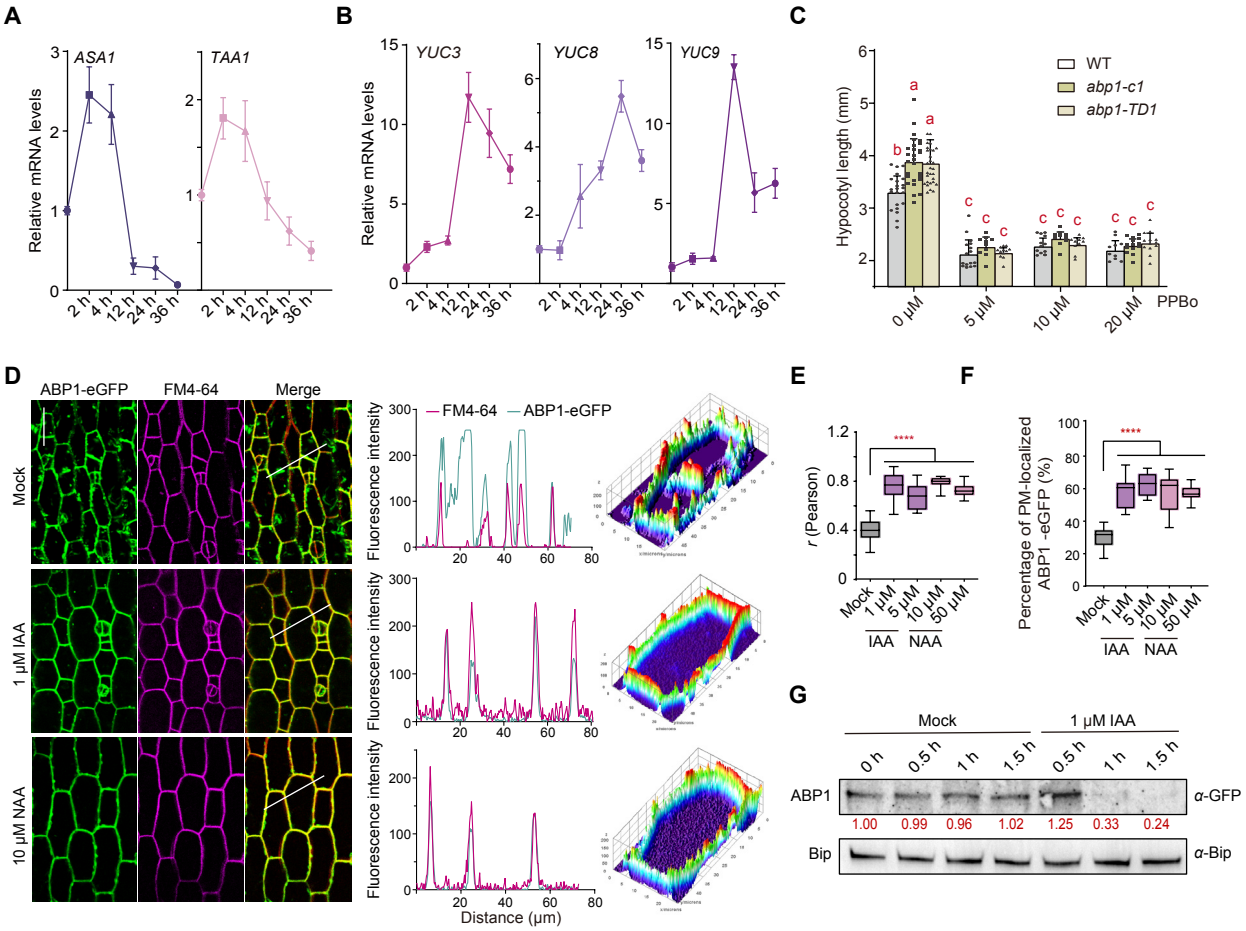

Figure 2. Dark treatment induces ABP1 trafficking through auxin biosynthesis in hypocotyl

(A–B) RT-qPCR analysis of *ASA1*, *TAA1*, *YUC3*, *YUC8* and *YUC9* in aboveground part of 4-day-old seedlings subjected to darkness for 0, 2, 4, 12, 24 or 36 h. Transcript levels were expressed as fold change relative to 0 h (set to 1).

(C) Quantification of hypocotyl length in 4-day-old light-grown *abp1-c1* and *abp1-TD1* seedlings followed by 36 h co-treatment of dark and auxin inhibitor targeting *YUCCA*s, PPBo. $n \geq 10$ hypocotyls.

(D) Confocal microscopy images (left), fluorescence plot profiles (middle), and 3D surface plots (right) of hypocotyl epidermal cells in 4-day-old seedlings treated with/without IAA or NAA for 1 h. FM4-64 labels the PM. White lines indicate fluorescence measurement regions. Scale bar, 20 μm.

(E) Pearson's coefficient of ABP1-eGFP and FM4-64 colocalization after IAA or NAA treatment for 1 h. $n \geq 13$ cells from 3–4 hypocotyls. (*r*), Pearson's colocalization coefficient.

(F) The percentage of PM-localized ABP1-eGFP in hypocotyl epidermal cells of 4-day-old seedlings with/without IAA or NAA treatments for 1 h. $n \geq 15$ cells from 3–4 hypocotyls.

(G) Western blot analysis of ABP1-eGFP protein levels following IAA treatment in ER fraction. *α*-Bip serves as ER marker. Red numbers indicate relative ABP1-eGFP protein levels at each time point relative to untreated control.

In (C, E–F), data are presented as mean ± SD. Significant differences were determined using two-way ANOVA (C). Different lowercase letters indicate significant differences at $P < 0.05$. Significant differences were determined using Student's *t*-test (E–F). ****$P < 0.0001$.

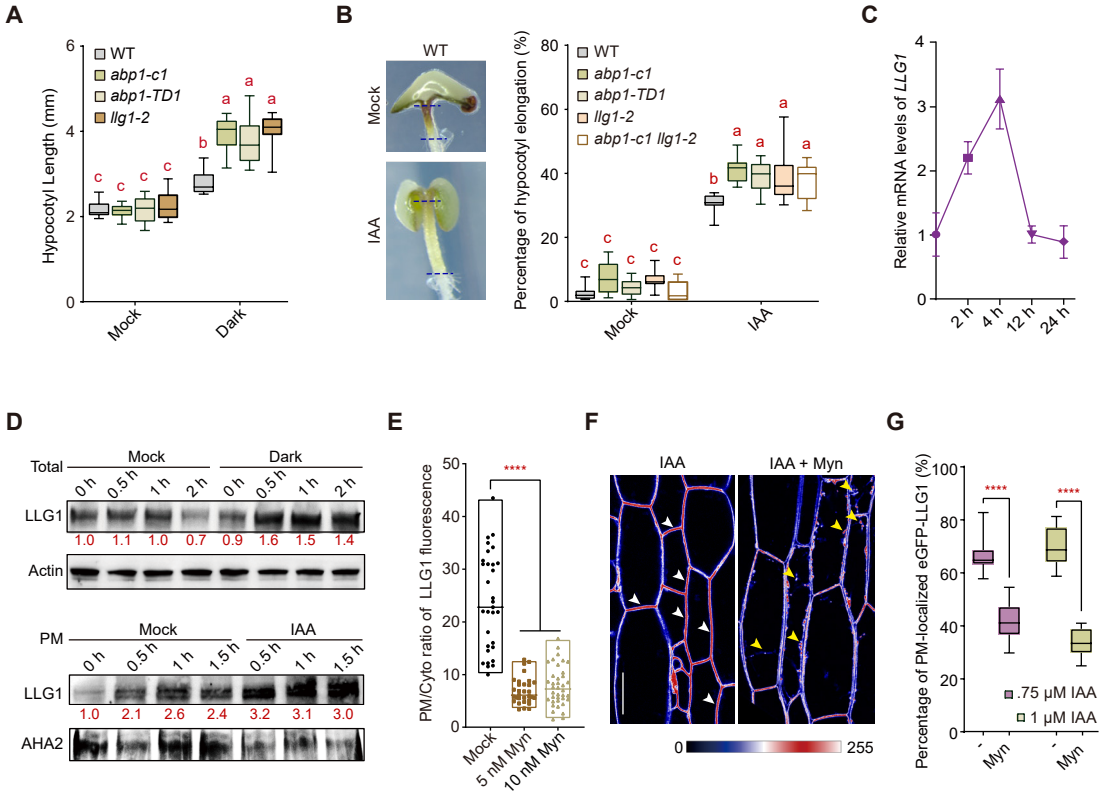

Figure 3. Dark-induced auxin stimulates the transcriptional expression of *LLG1*

(A) Quantification of hypocotyl length in 4-day-old WT, *abp1-c1*, *abp1-TD1 and llg1-2* seedlings subjected to dark treatment for 36 h. $n \geq 10$ hypocotyls.

(B) Schematic illustration of the lanolin paste application and representative phenotypes of WT seedlings with or without 1 mM IAA treatment applied to the cotyledons. Quantification of hypocotyl elongation in 4-day-old light-grown WT, *abp1-c1*, *abp1-TD1*, *llg1-2* and *abp1-c1 llg1-2* seedlings with or without IAA treatment. $n \geq 9$ hypocotyls.

(C) RT-qPCR analysis of *LLG1* in aboveground tissues of 4-day-old seedlings subjected to darkness for 0–24 h. Transcription levels were indicated as fold change relative to 0 h (set to 1).

(D) Western blot analysis of eGFP-LLG1 protein levels under darkness and IAA treatment. Total protein levels of eGFP-LLG1 in 4-day-old seedlings subjected to darkness for the indicated periods are shown (top). Plasma membrane (PM) fractions were isolated and analyzed for eGFP-LLG1 protein levels after IAA treatment for the indicated periods (bottom), with α-AHA2 used as a PM marker. Numbers in red indicate the relative protein amount of eGFP-LLG1 at each time point compared with the non-treated sample.

(E) Quantification of PM/cytoplasm LLG1 fluorescence signal ratio of root hair in 3.5-day-old *pLLG1:sp-eGFP-LLG1* transgenic seedlings with/without Myn treatment.

(F) Confocal microscopy imaging of hypocotyl epidermal cells in 4-day-old seedlings treated with IAA alone or Myn co-treatment (pseudo-colored with UnionJack LUT). Scale bar, 20 μm.

(G) The percentage of PM-localized eGFP-LLG1 in hypocotyl epidermal cells of 4-day-old seedlings treated with IAA alone or Myn co-treatment.

In (A, B E–G), data are presented as mean ± SD. Significant differences were determined using two-way ANOVA (A, B). Different lowercase letters indicate significant differences at $P < 0.01$. Significant differences were determined using Student's *t*-test (E–G). ****$P < 0.0001$.

See also, Figure S3.

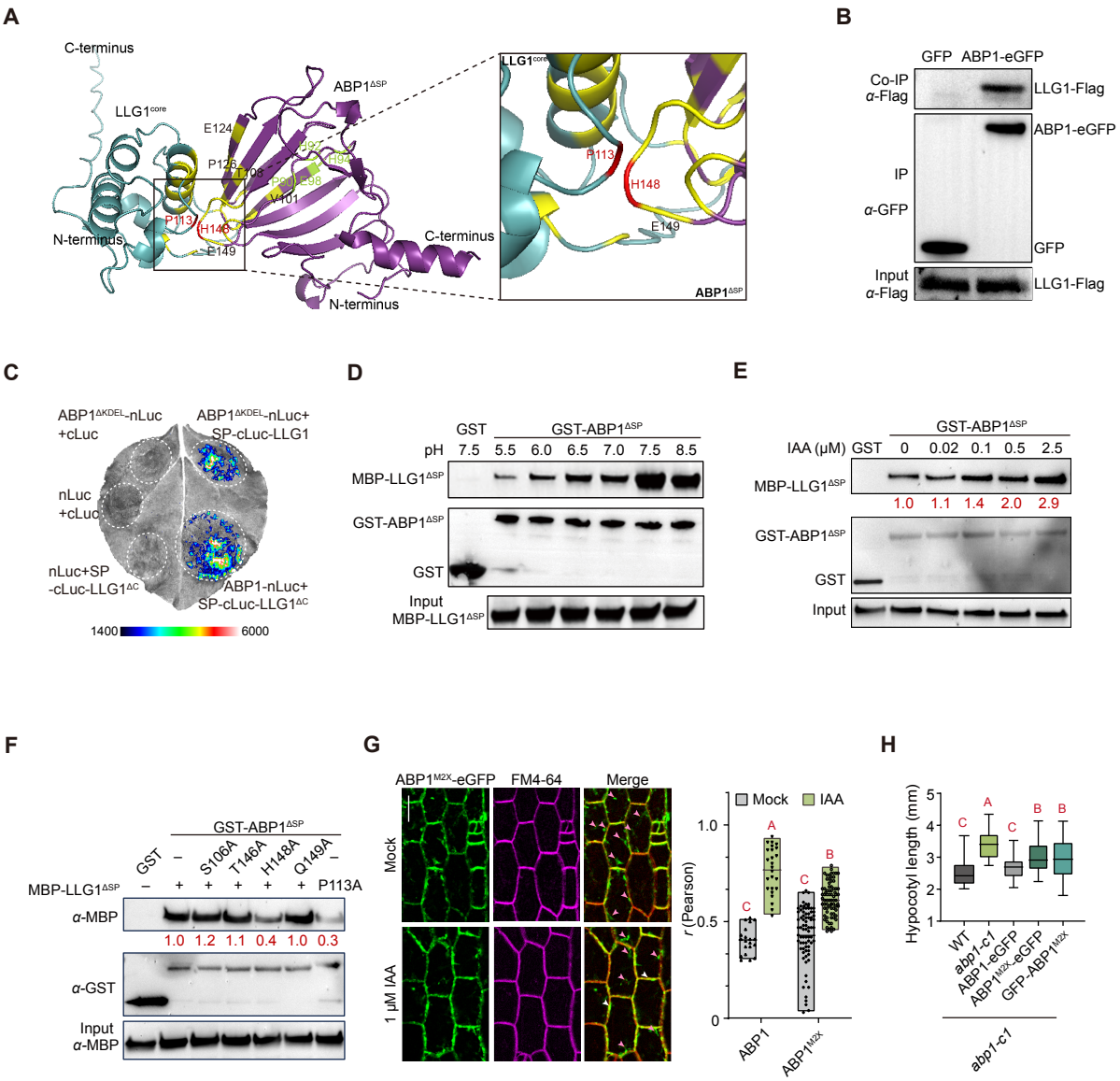

Figure 4. Auxin dose-dependently enhances the interaction between LLG1 and ABP1 in a pH-dependent manner

(A) AlphaFold3 protein interaction analysis of ABP1$^{\Delta SP}$ and LLG1^{core}. Yellow highlights the predicted ABP1$^{\Delta SP}$–LLG1^{core} interaction interface. The right panel shows an enlarged view of the interface, with LLG1^{core} shown in blue and ABP1$^{\Delta SP}$ shown in purple. The yellow region indicates the interaction interface and marks the 6 amino acid residues of ABP1$^{\Delta SP}$ involved in the predicted interaction. The green region highlights four key amino acid residues constituting the NAA-binding pocket. The orange region highlights W151, a key amino acid involved in the conformation of the C-terminus after binding of IAA.

(B) Co-IP of ABP1-eGFP and LLG1-Flag from the *pABP1:ABP1-eGFP pLLG1:sp-mCherry-LLG1-Flag* transgenic plants using anti-Flag antibody. ABP1-eGFP was detected by anti-GFP antibody.

(C) Luciferase complementation assay showing the interaction between ABP1$^{\Delta KDEL}$ and LLG1 or ABP1 and LLG1$^{\Delta C}$.

(D) Pull-down assay showing ABP1$^{\Delta SP}$–LLG1$^{\Delta SP}$ interaction under pH 5.5–pH 8.5.

(E) Pull-down assay showing ABP1$^{\Delta SP}$–LLG1$^{\Delta SP}$ interaction after IAA treatment under pH 7.5.

(F) Pull-down assay demonstrating interactions between: GST-ABP1^{Mut} (S106A, T146A, H148A, Q149A) and MBP-LLG1$^{\Delta SP}$ (Lane 3–6), GST-ABP1$^{\Delta SP}$ and MBP-LLG1^{P113A} (Lane 7) under pH 7.5.

(G) Fluorescence imaging and pearson's coefficient of hypocotyl epidermal cells in 4-day-old *pABP1:ABP1^{M2X}-eGFP/abp1-c1* seedlings treated with/without IAA for 1 h. White arrowheads indicate the colocalization signal. Pink arrowheads indicate the non-colocalization signal. (*r*), Pearson's colocalization coefficient. Scale bar, 40 μm.

(H) Quantification of hypocotyl length in 4-day-old WT, *abp1-c1*, *pABP1:ABP1-eGFP/abp1-c1*, *pABP1:GFP-ABP1^{M2X}/abp1-c1* and *pABP1:ABP1^{M2X}-eGFP/abp1-c1* transgenic plants subjected to darkness for 36 h. n ≥ 45 hypocotyls.

In (G–H), data are presented as mean ± SD. Significant differences were determined using one-way ANOVA. Different uppercase letters indicate significant differences at $P < 0.01$.

See also, Figure S4.

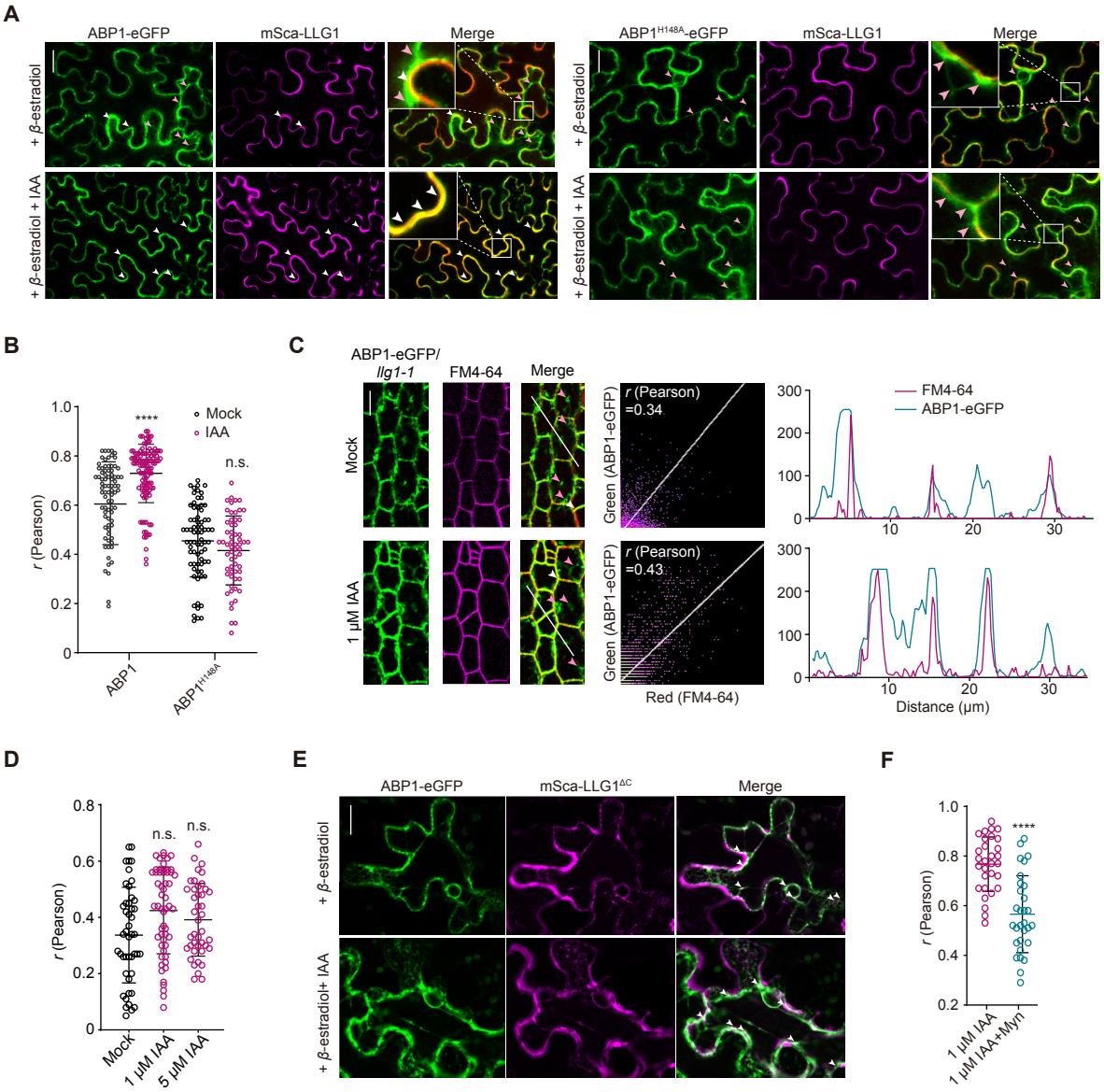

Figure 5. **LLG1 facilitates auxin-induced ABP1 trafficking from ER to PM**

(A–B) Fluorescence imaging and pearson's coefficient of ABP1 (or ABP1^{H148A}) and LLG1 in tobacco leaves. *pABP1:ABP1-eGFP* and *pER8:mSca-LLG1* were transformed to *N. benthamiana* leaves and treated with *β*-estradiol for 24 h and 1 μM IAA treatment for 35 min. Pink arrowheads indicate the ER regions. White arrowheads indicate the regions of colocalization. $n \geq 61$ cells.

(C) Confocal microscopy imaging (left), scatterplot analysis with Pearson's colocalization coefficient (middle) and fluorescence plot profiles (right) of ABP1-eGFP in *llg1-1* background in hypocotyl epidermal cells of 4-day-old seedlings with/without IAA treatment for 1 h. FM4-64 staining indicates the PM, white arrowheads indicate the colocalized signal; pink arrowheads indicate the non-colocalized signal.. White lines are used for fluorescence intensity measurement.

(D) Pearson's coefficient showing the colocalization of FM4-64 and ABP1-eGFP in *llg1-1* background after IAA treatment for 1 h. $n \geq 42$ cells from 15 hypocotyls.

(E) Fluorescence imaging of ABP1-eGFP with mSca-LLG1$^{\Delta C}$ co-expression in *N. benthamiana* leaves. *pABP1::ABP1-eGFP* and *pER8::mSca-LLG1$^{\Delta C}$* in *N. benthamiana* leaves were treated with *β*-estradiol for 24 h and 1 μM IAA treatment for 35 min. White arrowheads indicate the regions of colocalization.

(F) Pearson's coefficient of ABP1-eGFP and FM4-64 colocalization treated with IAA alone or Myn co-treatment. $n = 30$ cells.

Scale bars, 20 μm (A, E) and 10 μm (C). (*r*), Pearson's colocalization coefficient. In (B, D, F), data are presented as mean ± SD. Significant differences were determined using Student's *t*-test. n.s., not significant. ****$P < 0.0001$.

See also, Figure S5.

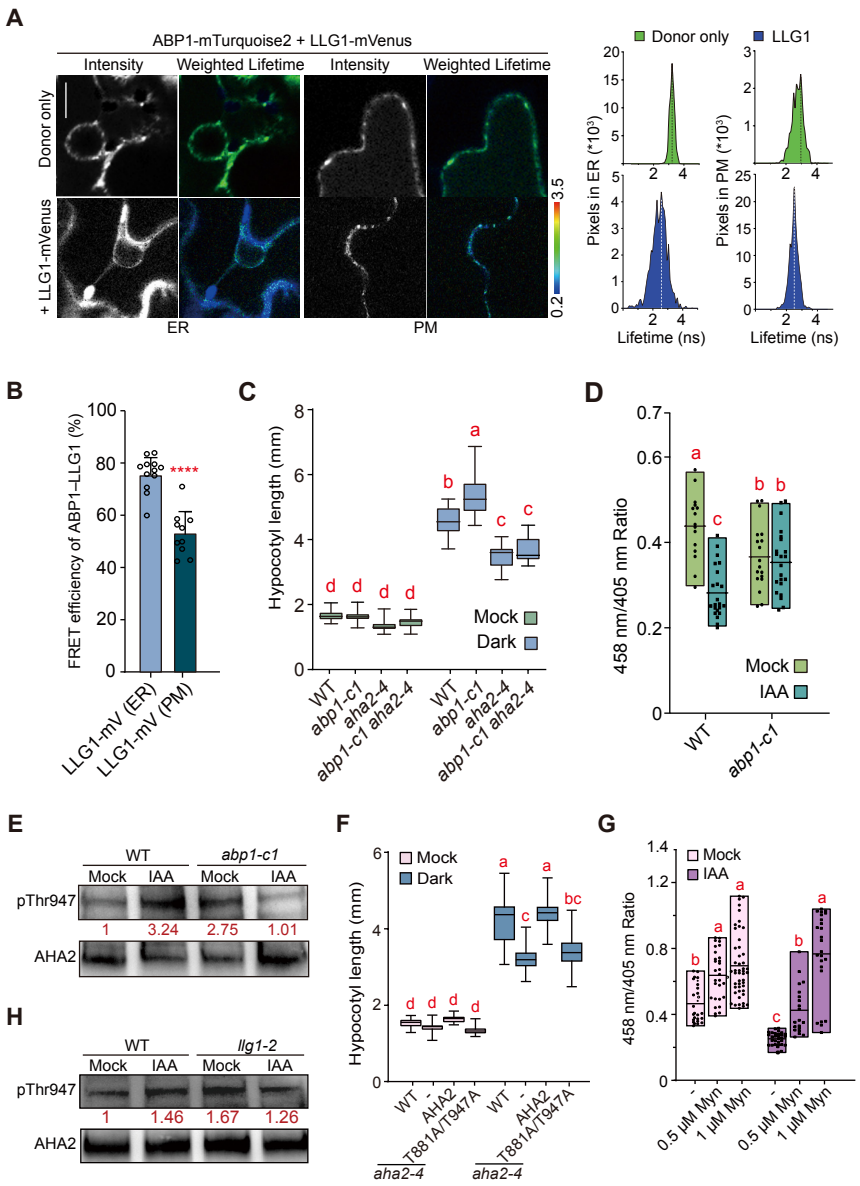

Figure 6. ABP1 regulates the AHAs-mediated dark-induced apoplast acidification and hypocotyl elongation

(A) Representative FRET-FLIM images (left), lifetime histograms (right) of the ABP1–LLG1 interaction at ER and PM. Intensity-weighted lifetime images use rainbow LUT pseudo-colouring. Histogram dashed lines mark peak lifetime values. Scale bar, 10 μm.

(B) Quantification of FRET efficiency of the ABP1–LLG1 interaction at ER and PM. $n \geq 10$ cells.

(C) Quantification of hypocotyl length in WT, *abp1-c1*, *aha2-4* and *abp1-c1 aha2-4* seedlings subjected to darkness for 30 h. $n \geq 23$ seedlings.

(D) Relative quantification of HPTS-stained apoplastic pH in hypocotyl cortex cells in 4-day-old WT and *abp1-c1* seedlings after dark treatment for 18 h following 1 μM IAA treatment for 15 min. $n \geq 15$ cells.

(E) Western blot detection of phosphorylated AHA2 in WT and *abp1-c1* seedlings (anti-pThr947). AHA2 protein levels were determined using anti-AHA2 antibodies. Seedlings were subjected to darkness for 12 h followed by 1 μM IAA treatment for 10 min.

(F) Quantification of hypocotyl length in *aha2-4*, *pAHA2::AHA2/aha2-4* and *pAHA2::AHA2*$^{T881A/T947A}$*/aha2-4* seedlings subjected to darkness for 30 h. $n \geq 20$ seedlings.

(G) Relative quantification of HPTS-stained pH in the apoplast of hypocotyl cortical cells in 3-day-old WT seedlings treated with Myn for 1 d followed by 18 h dark treatment and then 1 μM IAA treatment for 15 min. $n \geq 22$ cells.

(H) Western blot detection of phosphorylated AHA2 in WT and *Ilg1-2* seedlings (anti-pThr947). AHA2 protein levels were determined using anti-AHA2 antibodies. Seedlings were subjected to darkness for 12 h followed by 1 μM IAA treatment for 10 min.

In (B–D, F–G), data are presented as mean ± SD. Significant differences were determined using Student's *t*-test (B) or two-way ANOVA (C–D, F–G). **** $P < 0.0001$. Different lowercase letters indicate significant differences at $P < 0.05$.

See also, Figures S6 and S7.

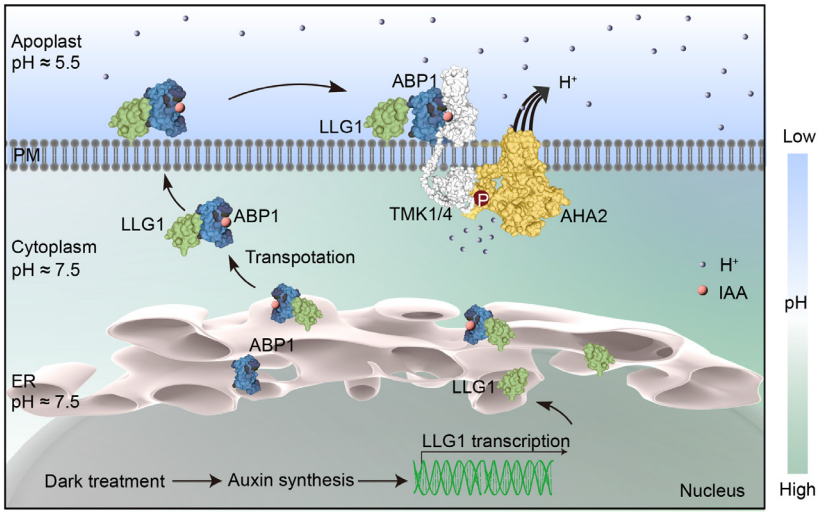

Figure 7. Model of dark/auxin-induced and LLG1-facilitated ABP1 trafficking in hypocotyl elongation

Dark treatment induces auxin biosynthesis and subsequently stimulates *LLG1* expression. Auxin enhanced LLG1 interaction with ABP1 in the ER and assists its trafficking through GPI-AP unique pathway. Upon reaching the PM, ABP1 dissociates from LLG1 under apoplastic acidic conditions and subsequently reassembled with the TMK receptor kinases to initiate proton ATPase-mediated signaling.

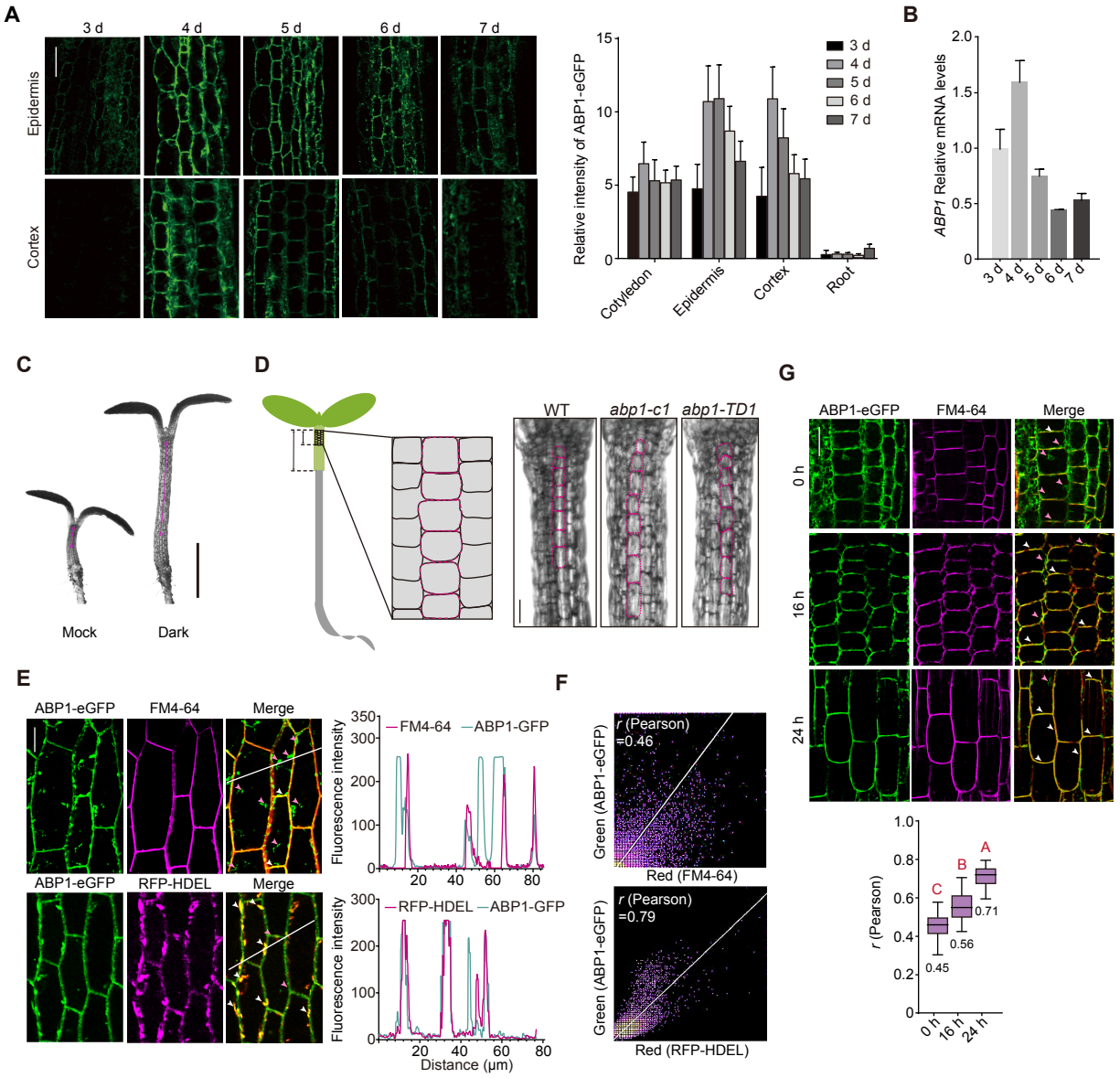

Figure S1. Auxin regulates hypocotyl elongation under dark condition, related to Figure 1

(A) Confocal microscopy imaging showing the expression of ABP1 in the hypocotyl of *pABP1::ABP1-eGFP* transgenic plants from day 3 to 7. Scale bar, 50 μm. Time-course analysis of the fluorescence intensity of ABP1-eGFP in cotyledon, hypocotyl epidermis, hypocotyl cortex and root. $n \geq 14$ seedlings.

(B) RT-qPCR analysis of *ABP1* expression in aboveground part of seedlings from day 3 to 7.

(C) Representative images of hypocotyl cell segment under double-point tracking. Red lines indicate the tracking region. Scale bar, 1 mm.

(D) Schematic representation of the hypocotyl cell region examined during this study. Phenotype of hypocotyl cell areas in 4-day-old WT, *abp1-c1* and *abp1-TD1* seedlings subjected to darkness for 30 h. Scale bar, 100 μm.

(E) Confocal microscopy imaging (left) and fluorescence plot profiles (right) of ABP1-eGFP in hypocotyl epidermal cells of 4-day-old seedlings. FM4-64 staining indicates the PM. RFP-HDEL indicates the ER. White arrowheads indicate the colocalization signal. Pink arrowheads indicate the non-colocalization signal. White lines are used for fluorescence intensity measurement. Scale bar, 20 μm.

(F) Scatterplot analysis of ABP1-eGFP colocalization with FM4-64 or RFP-HDEL in (E). (*r*), Pearson's colocalization coefficient.

(G) Confocal microscopy imaging of ABP1-eGFP in hypocotyl cortical cells of seedlings subjected to dark treatment for 16 or 24 h. Pearson's coefficient showing the colocalization of ABP1-eGFP and FM4-64-stained PM. (*r*), Pearson's colocalization coefficient. White arrowheads indicate the colocalized signal. Pink arrowheads indicate the non-colocalized signal. $n \geq 15$ cells from 3 hypocotyls. Scale bar, 40 μm. Data are presented as mean ± SD. Significant differences were determined using one-way ANOVA. Different uppercase letters indicate significant differences at $P < 0.01$.

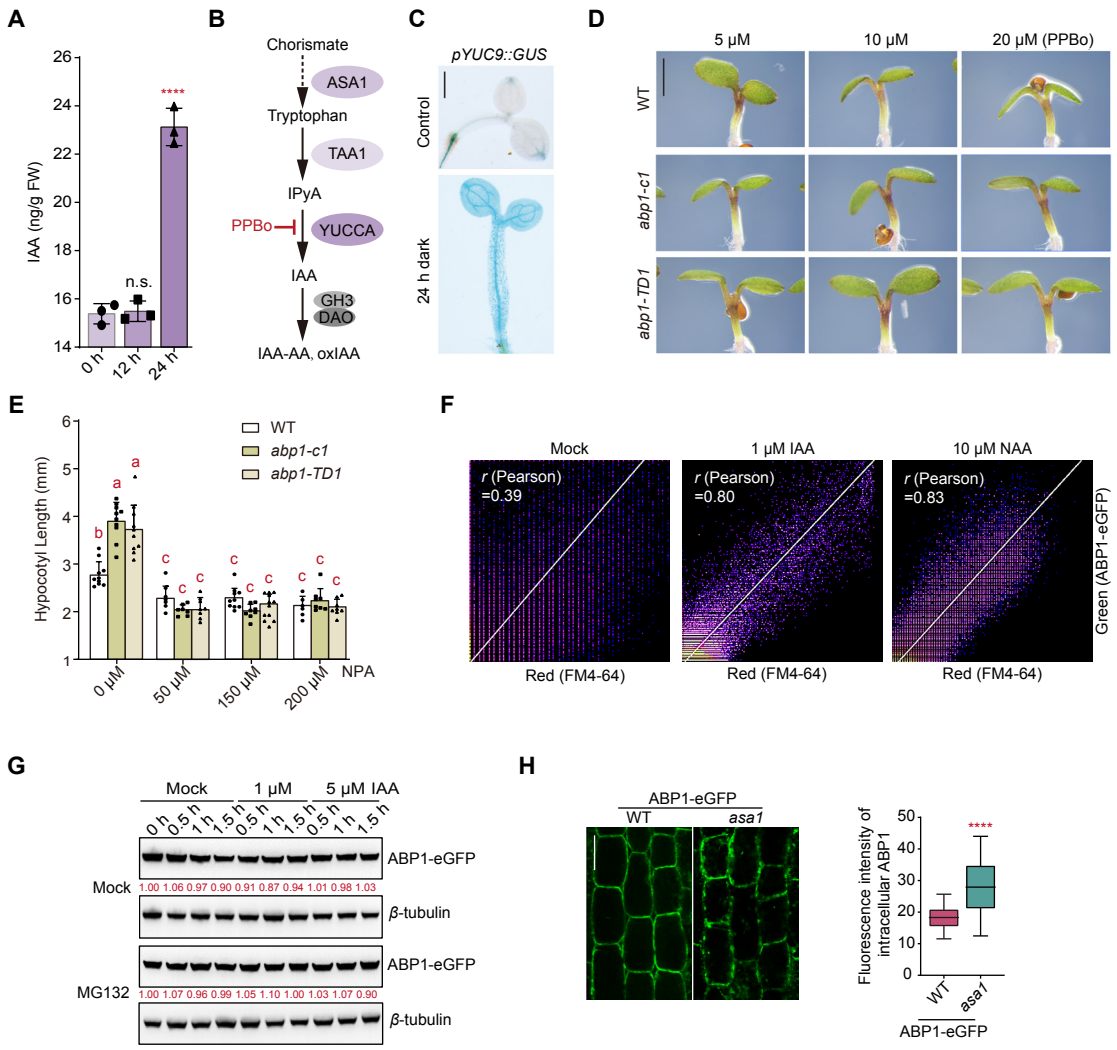

Figure S2. Dark treatment induces the trafficking of ABP1 through auxin, related to Figure 2

(A) Free IAA contents in aboveground tissue of 4-day-old seedlings subjected to darkness for 12 or 24 h. Data are presented as mean ± SD. Significant differences were determined using Student's *t*-test. ****$P < 0.0001$; n.s., not significant.

(B) Schematic representation of auxin biosynthesis pathway involving ASA1, TAA1 and YUCCA enzymes, with YUCCA activity inhibited by PPBo.

(C) GUS staining in 4-day-old *pYUC9::GUS* transgenic seedlings under normal light conditions (top) and after 24 h dark treatment (bottom). Scale bar, 1 mm.

(D) Phenotype of 4-day-old light-grown WT, *abp1-c1* and *abp1-TD1* seedlings followed by 36 h co-treatment of darkness and PPBo. Scale bar, 2 mm.

(E) Quantification of hypocotyl length in 4-day-old light-grown *abp1-c1* and *abp1-TD1* seedlings followed by 36 h co-treatment of dark and auxin inhibitor targeting *PIN*s, NPA. $n \geq 7$ hypocotyls.

(F) Scatterplot analysis of ABP1-eGFP and FM4-64 colocalization after IAA or NAA treatment. $n \geq 13$ cells from 3–4 hypocotyls. (*r*), Pearson's colocalization coefficient.

(G) Western blot showing the total protein levels of ABP1-eGFP in 4-day-old seedlings after IAA treatment at indicated period, with MG132 treatment as control. Numbers in red indicate protein amount of ABP1-eGFP after IAA treatment at each time point relative to non-treatment sample.

(H) Confocal microscopy imaging of ABP1-eGFP and fluorescence intensity of intracellular ABP1 in hypocotyl cortical cells of WT and *asa1* seedlings subjected to darkness for 18 h. Scale bar, 50 μm.

In (E, H), Data are presented as mean ± SD. Significant differences were determined using two-way ANOVA (E). Different lowercase letters indicate significant differences at $P < 0.05$. Significant differences were determined using Student's *t*-test (H). ****$P < 0.0001$.

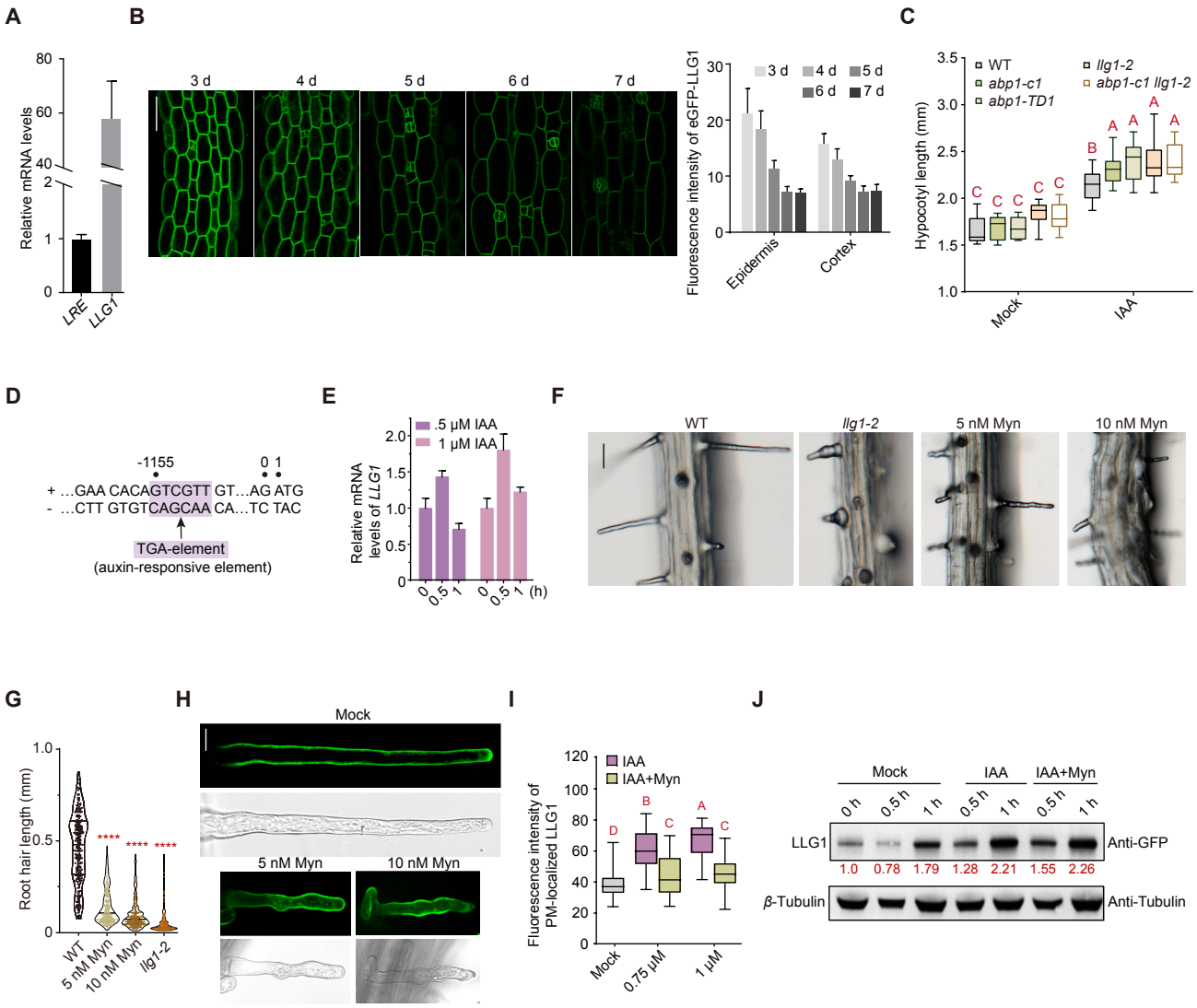

Figure S3. LLG1 promotes hypocotyl elongation via auxin signaling and Myn proteins restrain its trafficking, related to Figure 3

(A) RT-qPCR analysis of *LRE* and *LLG1* expression in the hypocotyl of 4-day-old seedlings.

(B) Confocal imaging showing the expression of LLG1 in hypocotyl cortical cells of *pLLG1:sp-eGFP-LLG1* transgenic plants from day 3 to 7. Scale bar, 50 μm. $n \geq 22$ seedlings. Time-course analysis of the fluorescence intensity of eGFP-LLG1 in hypocotyl epidermis and hypocotyl cortex from day 3 to 7.

(C) Quantification of hypocotyl length in WT, *abp1-c1*, *abp1-TD1*, *llg1-2* and *abp1-c1 llg1-2* seedlings under mock or IAA treatment for 12 h. $n \geq 9$ hypocotyls.

(D) Prediction in the *LLG1* promoter region showing an auxin-responsive element (TGA element).

(E) RT-qPCR analysis of *LLG1* expression in 4-day-old seedlings after IAA treatment for 0.5 or 1 h.

(F–G) Phenotype and quantification of root hair length in 3.5-day-old WT (with/without Myn treatment) and *llg1-2* (untreated) seedlings. Scale bar, 50 μm. $n \geq 149$ root hairs from 10 roots.

(H) LLG1 localization in root hair of 3.5-day-old *pLLG1:sp-eGFP-LLG1* transgenic seedlings with/without Myn treatment. Scale bar, 20 μm.

(I) Quantification of fluorescence intensity of PM-localized eGFP-LLG1 in hypocotyl epidermal cells of 4-day-old *pLLG1::sp-eGFP-LLG1* transgenic seedlings treated with IAA alone or together with Myn. $n \geq 12$ cells from 3–4 hypocotyls.

(J) Western blot showing the total protein levels of eGFP-LLG1 in 4-day-old seedlings treated with 1 μM IAA alone or Myn co-treatment. Numbers in red indicate protein amount of eGFP-LLG1 after treatment at each time point relative to non-treatment sample.

In (C, G, I), data are presented as mean ± SD. Significant differences were determined using two-way ANOVA (C, I). Different uppercase letters indicate significant differences at $P < 0.01$. Significant differences were determined using Student's *t*-test (G). ****$P < 0.0001$

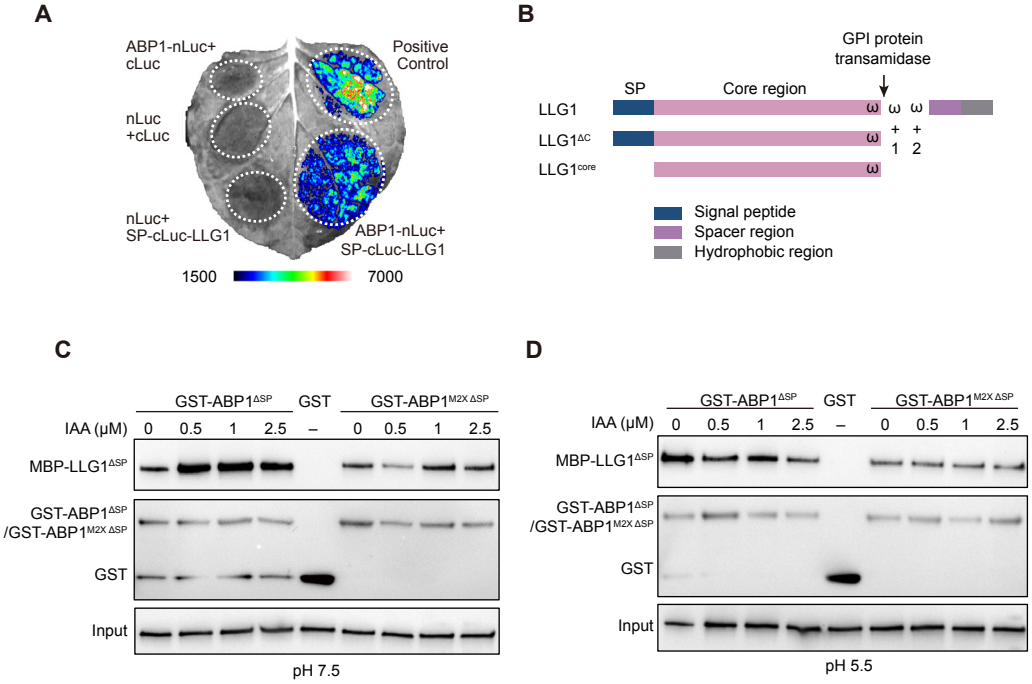

Figure S4. ABP1 and LLG1 exhibit direct physical interaction, related to Figure 4

(A) Luciferase complementation assay showing the interaction between full-length ABP1 and full-length LLG1. SP, signal peptide.

(B) The *LLG1* gene model, illustrating the predicted protein features, including the N-terminal signal peptide and the C-terminal GPI-anchor processing sites (ω-sites).

(C–D) Pull-down assay showing ABP1$^{\Delta SP}$–LLG1$^{\Delta SP}$ or ABP1$^{M2X\ \Delta SP}$–LLG1$^{\Delta SP}$ interaction after IAA treatment under pH 7.5 or pH 5.5.

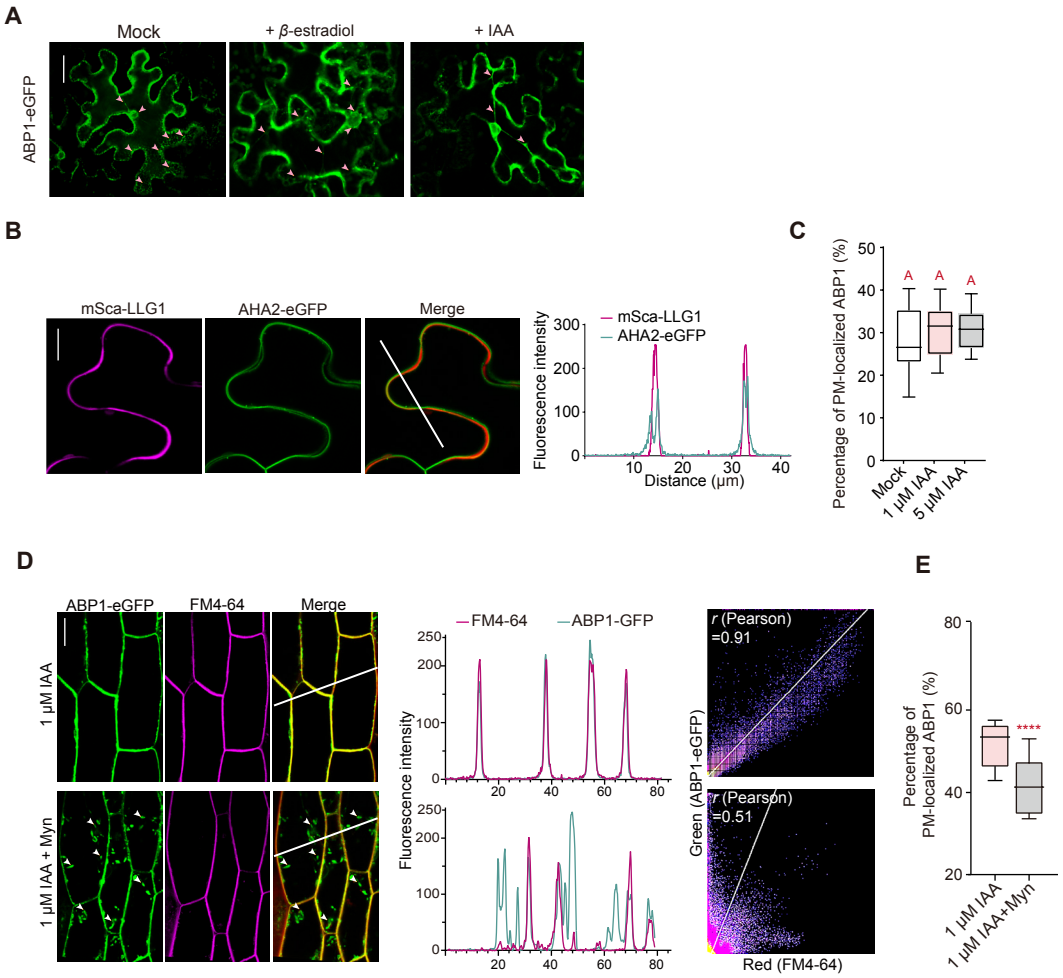

Figure S5. LLG1 chaperones ABP1 transportation through GPI-AP pathway, related to Figure 5

(A) Fluorescence imaging showing the expression of ABP1-eGFP alone under mock condition and treated with *β*-estradiol for 24 h or 1 μM IAA for 35 min in *N. benthamiana* leaves. Pink arrowheads indicate the ER regions. Scale bar, 20 μm.

(B) Confocal microscopy imaging and fluorescence plot profiles of mSca-LLG1 and PM marker AHA2-eGFP. White line indicates the region for fluorescence intensity measurement. Scale bar, 10 μm.

(C) The percentage of ABP1-eGFP localized to PM showing the colocalization of FM4-64 and ABP1-eGFP in *llg1-1* background after IAA treatment for 1 h. $n \geq 42$ cells from 15 hypocotyls.

(D) Confocal microscopy imaging (left), fluorescence plot profiles (middle) and scatterplot analysis with Pearson's colocalization coefficient (right) of ABP1-eGFP in hypocotyl epidermal cells of 4-day-old seedlings treated with IAA alone or Myn co-treatment for 1 h. White lines are used for fluorescence intensity measurement. White arrowheads indicate the punctate signals in ER. Scale bar, 20 μm.

(E) The percentage of ABP1-eGFP localized to PM relative to total protein in 4-day-old seedlings treated with IAA alone or Myn co-treatment. $n = 5$ hypocotyls.

In (C, E), data are presented as mean ± SD. Significant differences were determined using one-way ANOVA (C) or Student's *t*-test (E). Different uppercase letters indicate significant differences at $P < 0.01$. ****$P < 0.0001$.

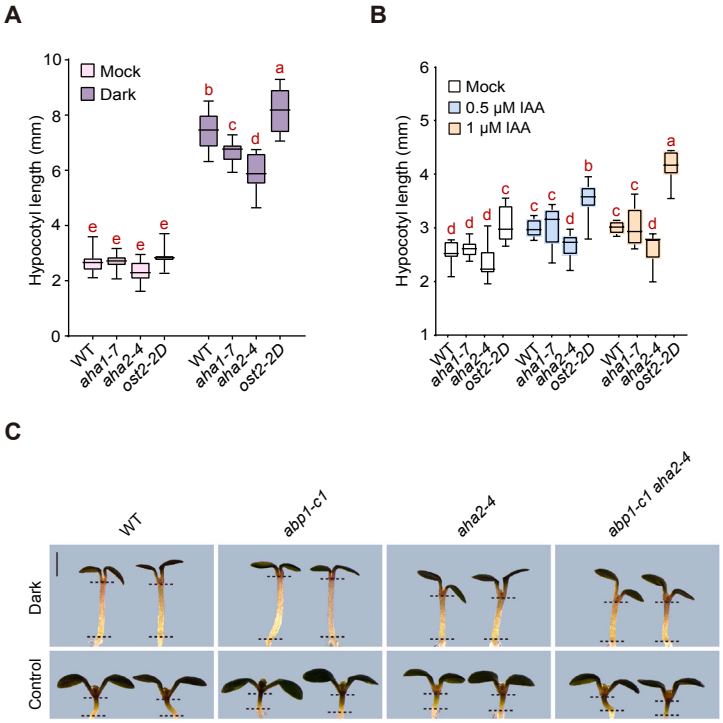

Figure S6. **AHA1/2 regulate hypocotyl elongation under dark and auxin treatment, related to Figure 6**

(A) Quantification of hypocotyl length in *aha1-7*, *aha2-4* and *ost2-2D* seedlings subjected to darkness treatment for 30 h. $n \geq 16$ seedlings.

(B) Quantification of hypocotyl length in *aha1-7*, *aha2-4* and *ost2-2D* seedlings treated with/without IAA for 30 h. $n \geq 7$ seedlings.

(C) Phenotype of hypocotyl length in WT, *abp1-c1*, *aha2-4* and *abp1-c1 aha2-4* seedlings subjected to darkness for 30 h. $n \geq 23$ seedlings. Scale bar, 2 mm.

In (A–B), data are presented as mean ± SD. Significant differences were determined using two-way ANOVA. Different lowercase letters indicate significant differences at $P < 0.05$.

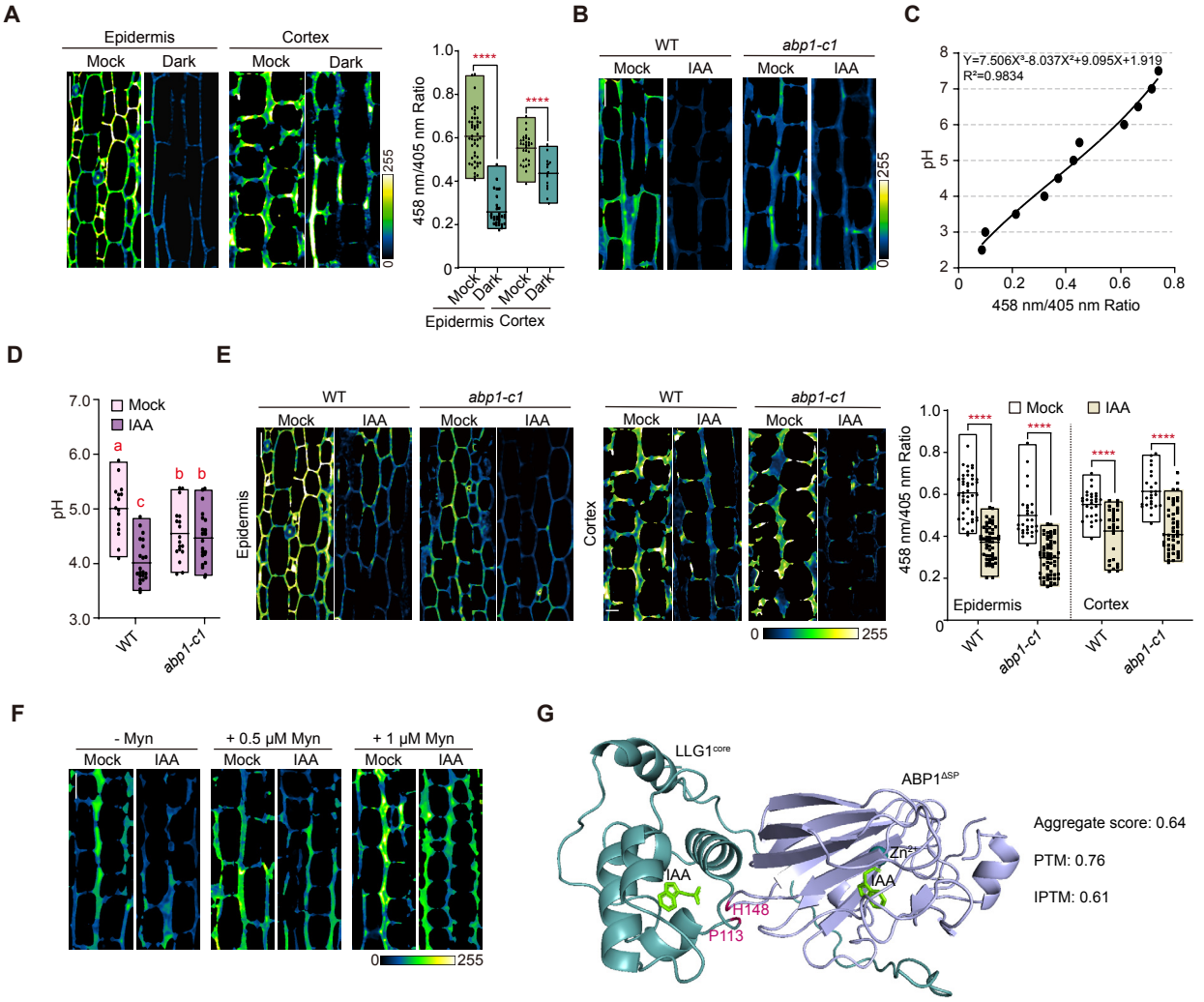

Figure S7. ABP1 regulates dark-induced apoplast acidification in hypocotyl, related to Figure 6

(A) Confocal imaging and relative quantification of HPTS-stained apoplastic pH in hypocotyl epidermal and cortical cells in 4-day-old WT seedings subjected to darkness for 18 h. $n \geq 15$ cells. Scale bar, 40 μm.

(B) Confocal imaging of HPTS-stained apoplastic pH in hypocotyl cortex cells in 4-day-old WT and *abp1-c1* seedlings after dark treatment for 18 h following 1 μM IAA treatment for 15 min. Scale bar, 40 μm.

(C) *In vivo* calibration curve of apoplastic pH.

(D) Relative quantification of apoplastic pH in hypocotyl cortical cells of 4-day-old WT and *abp1-c1* seedlings subjected to darkness for 18 h, followed by 1 μM IAA treatment for 15 min. HPTS-stained pH values were calculated using a standard curve.

(E) Confocal imaging and relative quantification of HPTS-stained pH in the apoplast of hypocotyl epidermal and cortical cells in 4-day-old light-grown WT and *abp1-c1* seedlings treated with 1 μM IAA for 15 min. $n \geq 25$ cells. Scale bar, 40 μm.

(F) Confocal imaging of HPTS-stained pH in the apoplast of hypocotyl cortical cells in 3-day-old WT seedlings treated with Myn for 1 d followed by 18 h dark treatment and then 1 μM IAA treatment for 15 min. Scale bar, 40 μm.

(G) Structural model of the LLG1–ABP1 interaction in the presence of IAA predicted by Chai-1 docking. $LLG1^{core}$ protein is colored deep teal and $ABP1^{\Delta SP}$ is colored light blue. The auxin molecule IAA is shown in green. The predicted key residues P113 in LLG1 and H148 in ABP1 are highlighted in hot pink.

In (A, D–E), data are presented as mean ± SD. Significant differences were determined using Student's *t*-test (A, E) or two-way ANOVA (D). ****$P < 0.0001$. Different lowercase letters indicate significant differences at $P < 0.05$.

580 **STAR METHODS**

581 Detailed methods are provided in the online version of this paper and include the following:

582 KEY RESOURCES TABLE

583 RESOURCE AVAILABILITY

584 Lead contact

585 Materials availability

586 Data and code availability

587 EXPERIMENTAL MODEL AND SUBJECT DETAILS

588 Plant Material and Growth Conditions

589 METHOD DETAILS

590 Dark treatment and hypocotyl growth examination

591 Auxin treatment and hypocotyl length measurement

592 Measurement of free IAA levels

593 Histochemical GUS staining assay

594 Plasmid construction and generation of transgenic plants

595 Plant protein extraction and western blot

596 RNA isolation, RT-PCR, and qRT-PCR analysis

597 Confocal microscopy imaging

598 Colocalization analysis

599 Luciferase complementation assay

600 Protein expression and purification

601 Pull-down assays

602 FRET-FLIM assay

603 HPTS staining and imaging

604 *In vivo* phosphorylation assay

605 Protein structure prediction and small-molecule docking

606 QUANTIFICATION AND STATISTICAL ANALYSIS

607 **SUPPLEMENTAL INFORMATION**

608 **ACKNOWLEDGMENTS**

The project was supported by grants from National Natural Science Foundation of China (32425008, 32230009, 32500276) and Science and Technology Commission of Shanghai Municipality (24N12800100). We express our sincere gratitude to Dr. Peng Zhang and Dr. Xue Zhang for assistance with structural prediction analysis; Dr. Lin Li and the Large-Scale Instrument Sharing Platform of the School of Life Sciences at Fudan University for support with hypocotyl growth kinetic analysis. We thank Dr. Jiří Friml for providing the seeds of *pABP1:GFP-ABP1-M2X*/*abp1-c1*, Dr. Lin Xu for *abp1-c1* and *abp1-TD1,* Dr. Jun Liu for *ost2-2D,* Dr. Meng-xiang Sun for RFP-HDEL and Dr. Peng Zhao for mScarlet-K32 vector. We also acknowledge the Institute of Genetics and Developmental Biology, CAS for IAA quantification assay and the Materials Characterization Center and the Instruments Sharing Platform of School of Life Sciences, East China Normal University.

AUTHOR CONTRIBUTIONS

C. L. conceived and supervised the project. J.W. conducted all experiments. J-P.Y. conducted genotyping, AHA-related analysis. C.L., J.W. and J-P.Y. prepared the manuscript. M-M.Z. and Y-Z.H. conducted GPI-AP trafficking analysis. H-Q.F. and M-Z.L. conducted initial ABP1-LLG1 functional analysis. T-D.X. contributed to the mechanistic interpretation and edited manuscript. B-Y.L. contributed to the preliminary investigation for this project.

DECLARATION OF INTERESTS

The authors declare no conflict of interest.

STAR METHODS

KEY RESOURCES TABLE

RESOURCE AVAILABILITY

Lead contact

Requests for further information and resources should be directed to and will be fulfilled by the lead contact, Chao Li (cli@bio.ecnu.edu.cn).

Materials availability

The *Arabidopsis* genetic transformation materials constructed in this study are available upon request.

Data and code availability

Data supporting the findings of this study are available within the paper. Source data (all gels and graphs) are provided with this paper. This study did not generate any code information.

EXPERIMENTAL MODEL AND STUDY PARTICIPANT DETAILS

Plant materials and growth conditions

Arabidopsis ecotype Col-0 was used as wild type in this study. The *abp1-c1*, *abp1-TD1(Gao et al., 2015)*, *llg1-2*(Li et al., 2015), *aha1-7*, *aha2-4(Liu et al., 2025a)*, *ost2-2D(Sylvain Merlot, 2007)*and *pYUC9:GUS(Chen et al., 2016)* have been described previously. Seeds were surface-sterilized with 75% (v/v) ethanol for 5 min, followed by five times washes with sterilized distilled water. The sterilized seeds were then germinated on plates containing half-strength Murashige and Skoog (1/2 MS) medium supplemented with 1% (w/v) sucrose and solidified with 0.8% (w/v) agar, adjusted to pH 5.7. *Arabidopsis* seedlings were cultivated in Percival growth chambers under controlled environmental conditions (hereafter, standard growth conditions): 16-h light/8-h dark photoperiod with 22℃ light/20℃ dark temperatures and 60% relative humidity. The light regimes were implemented under regular white light at an intensity of 100 μmol m^{-2} s^{-1}.

METHOD DETAILS

Dark treatment and hypocotyl growth examination

The kinetics of hypocotyl growth were monitored using the high-throughput imaging platform DynaPlant® at the School of Life Sciences, Fudan University. Seeds were sown on 1/2 MS medium solidified with 2% phytagel (Solarbio, P8170). 3-day-old seedlings were pretreated under continuous white light for 24 h for acclimation to fresh medium, and subsequently transferred to complete darkness for 36 h. During dark incubation, hypocotyl growth was imaged at 15 min intervals using the DynaPlant® system with a spatial resolution of 1.2 μm per pixel. Hypocotyl growth lengths in the time-series images were quantified by DynaPlant Analysis software (provided by the instrument manufacturer). Data are presented as mean ± SEM. Means were calculated from hypocotyls of more than 28 seedlings. Experiments were performed with at least three biological replicates, with each replicate derived from distinct biological samples to

minimize batch effects.

Hypocotyl imaging was conducted using a stereomicroscope (Leica M205 FCA) and a fluorescence microscope (Leica DM2500) equipped with a 20× water-immersion objective. Hypocotyl length was measured in ImageJ from the axillary bud to the hypocotyl-root junction. For cellular analyses, individual cell areas were quantified by tracing cell boundaries using the polygon selection tool in ImageJ.

4-Phenoxyphenylboronic acid (Kakei et al., 2015) (PPBo, MedChemExpress, HY-76584) or N-1-Naphthylphthalamic acid (Yang et al., 2022) (NPA, MedChemExpress, HY-116425) was added to solid 1/2 MS medium at specified concentrations for dark treatment. 4-day-old seedlings grown under standard conditions were transferred to the respective plates, which were then wrapped in two layers of aluminum foil to ensure complete darkness and placed vertically in Percival growth chambers. Hypocotyl imaging and length measurement were performed as described above.

Auxin treatment and hypocotyl length measurement

Seedlings were treated with liquid 1/2 MS medium (1% sucrose, pH 5.7), supplemented with indicated concentrations of indole-3-acetic acid (IAA, Sigma-Aldrich, I2886). All treatments were performed in 1.5 mL Eppendorf tubes under standard growth conditions with continuous white light (~100 $\mu mol \cdot m^{-2} \cdot s^{-1}$). For IAA treatment of cotyledons, lanolin (Aladdin, L116309) was used as the medium, as outlined in established protocols (Bellstaedt et al., 2019). Briefly, lanolin was melted at 65°C, mixed with 1mM IAA (at the desired concentrations) or DMSO, and homogenized thoroughly. Seedlings were then vertically positioned (adaxial-side down) in the lanolin-IAA mixture to ensure uniform cotyledon coating before solidification. The treated seedlings were then transferred to 1/2 MS solid medium and cultured vertically under standard growth conditions. The means were calculated from at least 9 hypocotyls. Experiments were performed with at least three biological replicates, with each replicate derived from distinct biological samples to minimize batch effects.

Measurement of free IAA levels

Seedlings were grown for 4 days under standard conditions and then transferred to darkness for 0, 12 or 24 h. For the quantification of phytohormone IAA, approximately 200 mg mixture of cotyledon and hypocotyl tissues were harvested and spiked with 3 ng [$^{13}C_6$] IAA internal standard. Samples were subjected to extraction, purification, and methylation prior to analysis by selected-ion-monitoring GC-MS following established protocols (Barkawi et al., 2008). The measurement was performed as previously described (Sun et al., 2016) in the Institute of Genetics and Developmental Biology, Chinese Academy of Sciences.

Histochemical GUS staining assay

For GUS staining assay, seedlings were incubated in buffer containing 100 mM sodium phosphate buffer (pH 7.0), 10 mM EDTA, 0.1% (v/v) Triton X-100, 0.5 mM potassium ferricyanide, 0.5 mM potassium ferrocyanide and 1 mM X-Gluc at 37°C in darkness for 12 h, followed by incubation in 70% ethanol for 5 h with the ethanol replaced every hour. The samples were photographed under a

704 stereoscope (Leica M205 FCA).

705 **Plasmid construction and generation of transgenic plants**

706 Primers used in this study can be found in Table S1. Full-length ABP1 and LLG1 cDNAs were
707 PCR-amplified from Col-0 for subsequent cloning. For plant transformation, the genes were
708 cloned into *pCAMBIA1300* to generate *pLLG1:sp-eGFP-LLG1* and *pABP1:ABP1-eGFP*
709 constructs, which were subsequently introduced into *llg1-2* mutant and Col-0 plants respectively
710 using *Agrobacterium tumefaciens* (strain GV3101)-mediated floral dip transformation(Clough and
711 Bent, 2008). For protein interaction studies, the cDNAs were first cloned into *pDONR221* vectors
712 (*P3P2-ABP1* and *P1P4-LLG1*) using BP recombination, then recombined into the
713 pFRETtv-2in1-CC7 vector (Addgene 105116) to create the FRET reporter construct
714 *pFRET-ABP1-mTurquoise2–LLG1-mVenus*. Additionally, ABP1 was subcloned into *pGEX-6P-1*
715 for prokaryotic expression in *Escherichia coli* (Rosetta, BL21).

716 For *SP-cLuc-LLG1*, sequences encoding the signal peptide of LLG1 (residue 1–23), nLuc,
717 and the deleted signal peptide of LLG1 (residues 24–168) were amplified by PCR and cloned into
718 *pCAMBIA1300* driven by the 35S promoter using a ClonExpress II One Step Cloning Kit. For
719 *SP-cLuc-LLG1*$^{\Delta GPI}$, sequences encoding the signal peptide of LLG1 (residue 1–23), nLuc, and the
720 deleted cytoplasmic domain of LLG1 (residues 24–147) were amplified. For *ABP1-nLuc*,
721 sequences encoding the ABP1 (residues 1–198) was fused with cLuc. For *ABP1*$^{\Delta KDEL}$, sequences
722 encoding the ABP1 (residues 1–194) was fused with cLuc. Primers used in plasmid construction
723 are listed in Table 1 (Supporting Information).

724 For *sp-mScarlet-LLG1 (XVE),* sequences encoding the signal peptide of LLG1 (residue 1–23),
725 mScarlet, and the deleted signal peptide of LLG1 (residues 24–168) were amplified by PCR and
726 cloned into *pER8* vector of the *XVE* inducible system (Jianru Zuo, 2000) using a ClonExpress II
727 One Step Cloning Kit. In transgenic tobacco leaves, estradiol-activated *XVE* induces expression of
728 the *mScarlet* reporter gene driven by a target promoter consisting of eight copies of the LexA
729 operator fused upstream of the −46 35S minimal promoter.

730 For *pAHA2:AHA2/aha2-4*, full-length AHA2 cDNA was PCR-amplified from Col-0
731 seedlings for subsequent cloning. To generate the native promoter-driven complementation
732 construct, the AHA2 genomic fragment containing the promoter region and coding sequence was
733 cloned into the binary vector pCAMBIA1300 to produce *pAHA2:AHA2*. For the phospho-deficient
734 mutant construct *pAHA2:AHA2*$^{T881A/T947A}$*/aha2-4*, site-directed mutagenesis was performed to
735 substitute Thr881 and Thr947 with alanine residues (T881A and T947A). The mutated AHA2
736 fragment was then cloned into pCAMBIA1300 under the control of the native AHA2 promoter to
737 generate *pAHA2:AHA2*$^{T881A/T947A}$. The resulting constructs were introduced into the *aha2-4* mutant
738 background via Agrobacterium tumefaciens (strain GV3101)-mediated floral dip transformation,
739 and transgenic lines were selected on hygromycin-containing medium for further analysis.

740 **Plant protein extraction and western blot**

741 For the detection of changes in protein levels, plant tissue samples from specific periods and
742 treatments were harvested and ground in liquid nitrogen. Total proteins were extracted using
743 Tris-HCl buffer (pH 6.8) through sequential centrifugation (15,000 × g, 30 min; then 15,000 × g,
744 10 min) at 4°C. For MG132 (MedChemExpress, HY-13259) treatment, it was diluted with 1/2 MS

745 liquid medium to 30 μM and applied 30 min prior to IAA treatment. Protein samples were
746 quantified by BCA assay, mixed with loading buffer, and heat-denatured at 99°C for 10 min.

747 Plasma membrane (PM) proteins were extracted using a commercial kit (Solarbio, China,
748 EX2080). Protease inhibitor cocktail (2 μL) was added to 500 μL of cold Extraction Buffer A,
749 mixed thoroughly, and kept on ice. Plant tissue (100–200 mg) was finely chopped and
750 homogenized in 500 μL of Extraction Buffer A at 2–8°C. The homogenate was transferred to a
751 pre-cooled centrifuge tube, shaken at 2–8°C for 30–60 min, and then centrifuged at 12,000 × g for
752 5 min at 2–8°C. The supernatant was collected, mixed with 5 μL of Extraction Buffer B, incubated
753 at 37°C for 10 min, and centrifuged at 1,000 × g for 3 min at 37°C. After removing the upper layer,
754 the remaining 30–50 μL lower phase was dissolved in 50–150 μL ice-cold Membrane Protein
755 Solubilization Buffer C to obtain the membrane protein fraction.

756 Endoplasmic reticulum (ER) proteins were extracted using a commercial kit (Solarbio, China,
757 EX2061). Briefly, protease inhibitor cocktail was added to Extraction Buffer C (2 μL per 300 μL),
758 mixed, and kept on ice. Approximately 200–500 mg of plant tissue (de-veined and cleaned) was
759 finely chopped, homogenized in 1 mL Extraction Buffer A using a homogenizer or Dounce
760 homogenizer, and filtered through a 100 μm cell strainer. The filtrate was sequentially centrifuged
761 at 200 × g for 3 min, 500 × g for 5 min, 1000 × g for 10 min, and 20,000 × g for 10 min, collecting
762 the supernatant at each step. This was followed by ultracentrifugation at 50,000 × g for 45 min to
763 pellet microsomal membranes (using a benchtop ultracentrifuge, Thermo Sorvall MTX150). The
764 pellet was resuspended in 400 μL of cold Reagent B, centrifuged again at 50,000 × g for 45 min,
765 and the resulting pellet was resuspended in 200–300 μL of Extraction Buffer C. After shaking at
766 2–8 °C for 30 min, the mixture was centrifuged at 12,000 × g for 10 min at 4 °C. The supernatant
767 containing ER proteins was collected, quantified, aliquoted, and stored at −80 °C for further use.

768 For Western blot detection, anti-GFP (1:2000 dilution, sc-9996, Santa Cruz, America) was
769 used to detect eGFP-LLG1 or ABP1-eGFP fusion protein expression. Anti-Bip (1:2000 dilution,
770 Agrisera, AS09481, Sweden) was used as an ER reference protein. Anti-AHA2 (1:1000 dilution,
771 PY231, Beijing QiWei YiCheng Tech Co., Ltd) was used as a PM reference protein.
772 HRP-conjugated Goat Anti-Mouse IgG (1:5000 dilution, Sangon Biotech, D110087) or
773 HRP-conjugated Goat Anti-Rabbit IgG (1:5000 dilution, Sangon Biotech, D110058) was used as
774 the secondary antibody.

775 **RNA isolation, RT-PCR, and qRT-PCR analysis**

776 Seedlings at appropriate developmental stages were harvested, and roots were excised to retain
777 only aboveground parts for transcript profiling of *ABP1* and *LLG1/LRE* genes. RNA was extracted
778 using the RNAprep Pure Plant Kit (TIANGEN, China), and first-strand cDNA was synthesized
779 with a HiScript ®II 1st Strand cDNA Synthesis kit (Vazyme, China). qRT-PCR was performed
780 with ChamQ Universal SYBR qPCR Master Mix (Vazyme, China) using the following thermal
781 profile: 95°C for 5 min, 30 cycles of 95°C for 10 s and 60°C for 30 s. Relative transcript levels
782 were calculated using the $2^{-\Delta\Delta CT}$ method, normalized to *ACTIN2*. Primer sequences are listed in
783 Table 1 (Supporting Information).

784 **Confocal microscopy imaging**

785 For colocalization analysis in *Arabidopsis thaliana* and *N. benthamiana*, images were acquired by

786 the Ultra High Resolution Laser Leica STELLARIS 8 confocal microscope with WLL laser,
787 power HyD detector (HyDx, HyD2 and HyD3) and frame scanning mode. The real fluorescence
788 signal was determined using TauGating (time-gated fluorescence lifetime filtering) and counting
789 techniques as capture modes. TauGating was applied to suppress autofluorescence, and photon
790 counting mode was used to enhance signal-to-noise ratio (Kriechbaumer et al., 2018). No
791 fluorescence signal was detected in Col-0 seedlings under identical imaging settings and channels.
792 Intracellular ER was visualized using RFP-HDEL (Gomord V, 1997) as an ER marker, while PM
793 was stained with the lipophilic dye FM4-64 (Liu et al., 2024), allowing simultaneous visualization
794 of both compartments. For various fluorescent proteins, GFP, Ex 490 nm, Em 505–560 nm; RFP,
795 Ex 532nm, Em 550–700 nm; FM4-64, Ex 523nm, Em 550–700 nm; mScarlet, Ex 594, Em 628 nm.
796 All imaging sessions, including mock controls and experimental samples (IAA or NAA treatment;
797 NAA, Sigma-Aldrich, N0640), were acquired using identical instrument settings: laser power
798 (20% WLL output) and environmental conditions (21℃ with 35% humidity). The statistics were
799 calculated from more than 3 cells in approximately 3–4 independent hypocotyls. Each cell area
800 included the complete cell edge, and the same calculation parameters and procedures were used
801 for all cells. Experiments were performed with at least three biological replicates, with each
802 replicate derived from distinct biological samples to minimize batch effects.

803 Myriocin (Myn, GLPBIO, GC14278, Montclair, CA, USA) was added to the solid medium
804 for cultivating *Arabidopsis thaliana* seedlings. 10 μM *β*-estradiol (Sigma-Aldrich E2758) was
805 pressure-infiltrated into Agrobacterium-transformed tobacco leaves 24 h post-transformation, with
806 phenotypic analysis performed 24 h post-induction.

807 **Colocalization analysis**

808 Colocalization was quantified in Fiji software using the Coloc 2 plugin (Analyze › Colocalization
809 Analysis › Coloc 2), yielding colocalization scatter plots, Pearson coefficients. For each sample,
810 paired green and red channel images were loaded, and regions of interest (ROIs) were selected for
811 analysis. Pearson's correlation coefficients (*r*), ranging from −1 (perfect negative correlation) to
812 +1 (perfect positive correlation)(Adler and Parmryd, 2010), were calculated to quantify the degree
813 of signal colocalization. Pearson's correlation coefficients (*r*) were computed as follows:

814
$$r = \frac{\sum (R_i - R_{av}) \cdot (G_i - G_{av})}{\sqrt{\sum (R_i - R_{av})^2 \cdot \sum (G_i - G_{av})^2}}$$

815 R_i, G_i represent the intensity values of the i-th pixel in the red channel (R_i) and green channel (G_i).
816 R_{av}, G_{av} represent the mean intensities of the entire dataset for the red channel (R_{av}) and green
817 channel (G_{av}).

818 To obtain the colocalization peak plots, merged dual-fluorescence images were converted to
819 color channels: Image > color > channel tool > color channel. A straight line was used to mark the
820 region of interest, and the plot profile's live mode was employed to display the fluorescence peak
821 plots of different channels. The data were saved separately and graphed in GraphPad Prism.

822 **Luciferase complementation assay**

823 *Agrobacterium tumefaciens* strain GV3101 harboring various constructs was cultured in LB liquid
824 medium until reaching an OD_{600} of 1.0. The cultures were then centrifuged at 3,824 × g for 10 min,

825 and the resulting pellets were washed and resuspended in double-distilled water supplemented
826 with 10 mM MES (pH 5.7), 10 mM $MgCl_2$, 0.01% Tween-20 and 100 μM acetosyringone to a
827 final OD_{600} of 0.6. Equal volumes of bacterial suspensions containing the nLUC and cLUC
828 constructs were mixed and infiltrated into designated regions of *Nicotiana benthamiana* leaves.
829 Plants were kept in darkness for 12 h, then transferred to a 16-h light/8-h dark cycle for an
830 additional 48 h. To assess luciferase activity, infiltrated leaves were treated with a luciferin
831 solution [1 mM luciferin, 0.05% (v/v) Triton X-100] and incubated in the dark for 5 min, followed
832 by imaging using a Tanon-5200 Multi chemiluminescence/fluorescence imaging system (Tanon,
833 China) equipped with a cooled CCD camera.

834 **Protein expression and purification**

835 DNA sequences encoding LLG1 (residues 24–168) and ABP1 (residues 34–198) were cloned into
836 the pMAL-c5x or pGEX-6P-1 vectors for expression in *E. coli* BL21 Competent Cells. For MBP-
837 and GST-tagged proteins, cells were incubated at 37°C with shaking at 200 rpm until the OD_{600}
838 reached 0.6. Following induction with 0.5 mM isopropyl-*β*-d-thiogalactopyranoside (IPTG), cells
839 were incubated with shaking for 3 h at 37°C (MBP-LLG1) or 16 h at 25℃ (GST-ABP1), and
840 harvested by centrifugation at 3,824 × g for 10 min at 4°C. Cells were lysed by sonication on ice
841 in lysis buffer containing 50 mM Tris-HCl pH 7.5, 100 mM NaCl, 1 mM Na_2-EDTA, 5% (v/v)
842 glycerol , and 1 mM PMSF, and centrifuged at 15,000 rpm for 30 min at 4°C. The supernatants
843 were purified using amylose resin (YESEN, China) for MBP fusion protein and glutathione
844 agarose resin (YESEN, China) for GST fusion protein.

845 **Pull-down assays**

846 For the GST pull-down assay, purified MBP-LLG1$^{\Delta SP}$ and GST-ABP1$^{\Delta SP}$ (GST-ABP1$^{\Delta SP\ S106A}$,
847 GST-ABP1$^{\Delta SP\ T146A}$, GST-ABP1$^{\Delta SP\ H148A}$) proteins were resuspended in binding buffer (50 mM
848 Tris-HCl pH 5.5/6.0/6.5/7.0/7.5/8.5, 100 mM NaCl, 1 mM Na2-EDTA, 5% (v/v) glycerol, 1 mM
849 PMSF) and incubated with GSTSep Glutathione Agarose Resin (Yeasen, 20507ES10) at 4°C for 2
850 h with rotation. The resins were then washed three times in pull-down buffer, followed by the
851 addition of SDS-PAGE loading buffer and boiled for 5 min, and used for immunoblot analysis.
852 The protein blot was stained with Ponceau S for loading detection. Anti-MBP antibody
853 (D195305-0100, 1:2,000 dilution, Sangon Biotech, China), anti-GST horseradish
854 peroxidase-conjugated antibody (B-14, 1:1,000 dilution, Santa Cruz Biotechnology, USA), and
855 anti-mouse secondary antibody (ASS1007, 1:5,000 dilution, Abgent, USA) were used for
856 chemiluminescence detection. The signals were acquired using the Tanon-2500R imaging system
857 (China).

858 **FRET-FLIM assay**

859 Tobacco (*Nicotiana benthamiana*) leaves were agroinfiltrated to co-express ABP1-mTurquoise2
860 (donor) and LLG1-mVenus (acceptor) constructs. Imaging was performed 48–72 h
861 post-infiltration on epidermal cells exhibiting dual fluorescence signals. Confocal laser scanning
862 microscopy (CLSM) settings were as follows: excitation 458 nm/emission 465 to 505 nm
863 (mTurquoise2), excitation 514 nm/emission 520 to 560 nm (mVenus). Cells of interest were
864 selected using a 40 × water-immersion objective. ABP1-mTurquoise2 was used as the donor only.
865 The fluorescence lifetime of the donor (mTurquoise2) was measured using the FLIM (Bücherl et

al., 2014) module (PicoHarp 300 TCSPC system), with the average value obtained from three measurements as the initial fluorescence lifetime of the donor. The efficiency of mTurquoise2–mVenus FRET was analyzed using a STED Leica microscope with the FRET module. The region of interest (ROI) was selected to focus on the specific subcellular regions, and the initial fluorescence lifetime value of the donor was inputted. FRET efficiency was automatically calculated by the system using the following formula:

$$E_{(\mathrm{FRET-FLIM})} = 1 - \frac{\tau(\mathrm{quench})}{\tau} = 1 - \frac{\tau(\mathrm{donor, FRET})}{\tau(\mathrm{donor, no\ FRET})}$$

τ (donor, FRET) represents the donor lifetime in the presence of the acceptor, and τ (donor, no FRET) represents the donor lifetime in the absence of the acceptor(Bücherl et al., 2014).

HPTS staining and imaging

HPTS staining(Amali et al., 2011; Liu et al., 2025b) and imaging were performed as described by Lin(Lin et al., 2021) with modifications. Prior to staining, hypocotyls of 4-day-old light-grown seedlings or seedlings subjected to 18 h of darkness were equilibrated in 1/2 MS growth medium supplemented with 0.2 mM MES for at least 30 min. For auxin treatment, hypocotyls were incubated in 1/2 MS growth medium supplemented with 5 mM HPTS (prepared from a 100 mM aqueous stock solution) and 1 μM IAA for 15 min. For Myn treatment, seedlings were grown on 1/2 MS medium under continuous light for 3 days and then transferred to 1/2 MS solid medium supplemented with different concentrations of Myn for pre-incubation for 24 h. Subsequently, seedlings were subjected to co-treatment with Myn under dark conditions for 18 h, after which hypocotyls were incubated in 1/2 MS growth medium containing 5 mM HPTS and 1 μM IAA for 15 min. After staining, hypocotyls were mounted in the same growth medium on microscopy slides and covered with coverslips for imaging.

Hypocotyl imaging was performed using an Ultra High-Resolution Leica STELLARIS 8 confocal microscope equipped with a 20 × water-immersion objective. Fluorescence signals corresponding to the protonated form of HPTS were detected using excitation at 405 nm with an emission peak at 514 nm, while signals from the deprotonated form were detected using excitation at 458 nm with an emission peak at 514 nm.

For extracellular pH quantification, the ratio of fluorescence intensity excited at 458 nm to that excited at 405 nm (458/405 ratio) was calculated. Approximately 5–6 independent hypocotyls were analyzed per treatment, with about 2–3 cells analyzed per hypocotyl, resulting in a total of at least 15 cells per condition. Full cell boundaries were used for all measurements, and identical image processing parameters were applied across all samples.

For *in vivo* HPTS calibration, hypocotyls were equilibrated in a measuring buffer (5 mM MES, 5 mM citric acid, 5M KOH, pH 2.5–7.5) for 30 min. The hypocotyls were then incubated in the same buffer supplemented with 5 mM HPTS for 20 min. The hypocotyls were subsequently mounted on a microscopy slide with the same buffer, covered with a coverslip, and imaged using the same confocal settings as described above. A calibration curve was generated and pH values were determined by fitting experimental data with a polynomial function.

904 ***In vivo* phosphorylation assay**

905 For the *in vivo* phosphorylation assay, 4-day-old light-grown seedlings were first subjected to
906 darkness for 12 h, followed by 1 μM IAA treatment for 10 min and then harvested and flash
907 frozen in liquid nitrogen. Samples were ground into a fine powder in liquid nitrogen and
908 suspended in 2×SDS loading buffer (8% SDS, 100 mM Tris-HCl (pH6.8), 20% Glycerol, 0.02%
909 BPB) supplemented with protease inhibitor cocktail (A32955, Thermo Fisher Scientific, China).
910 The homogenates were boiled at 99℃ for 3 min and then centrifuged at 12,000 g for 10 min at
911 room temperature. Equal amounts of supernatant were loaded onto 4%–12% (w/v) SDS–PAGE
912 gels to assess the levels of AHA2 (anti-AHA2 1:1000 dilution, PY231, Beijing QiWei YiCheng
913 Tech Co., Ltd) and phosphorylation at Thr947 (anti-pThr947, 1:1500 dilution, ZW075213,
914 Abmart, China). Goat anti-rabbit IgG and goat anti-mouse IgG (1:5000 dilution) were used as
915 secondary antibodies. The signals were detected using the Tanon-2500R imaging system (Tanon,
916 China).

917 **Protein structure prediction and small-molecule docking**

918 Protein structure prediction and small-molecule docking were performed using AlphaFold3 (v.3)
919 (Abramson et al., 2024) and Chai-1 (v0.6.1) (Boitreaud et al., 2024), respectively, both in
920 multimeric mode with default parameters. Structural models were visualized using PyMOL
921 (v.3.0.3) (Shelton, 2025), and contact plots were generated using custom scripts. For AlphaFold
922 structural prediction, LLG1 (24–168 AA) and ABP1 (34–198 AA) (full length with the signal
923 peptide removed) were used. For Chai-1 docking analysis, LLG1 (24–149 AA) and ABP1
924 (34–198 AA) were used.

925 **QUANTIFICATION AND STATISTICAL ANALYSIS**

926 All experiments were independently repeated at least three times. Data are presented as mean ±
927 SD. Statistical analyses were performed using GraphPad Prism 8 software. In all graphs, asterisks
928 indicate statistical significance (n.s., not significant, $*P < 0.05$; $**P < 0.01$; $***P < 0.001$; $****P$
929 < 0.0001) tested by Student's *t*-test (two groups), and lowercase/uppercase letters indicate
930 statistical significance tested between multiple groups by one/two-way ANOVA at $P < 0.05$
931 (lowercase) or $P < 0.01$ (uppercase). The intensity of protein bands in Western blotting was
932 quantified using ImageJ software.

933 **References**

934 Abramson, J., Adler, J., Dunger, J., Evans, R., Green, T., Pritzel, A., Ronneberger, O., Willmore, L.,
935 Ballard, A.J., Bambrick, J., et al. (2024). Accurate structure prediction of biomolecular interactions
936 with AlphaFold 3. Nature *630*, 493-500. https://doi.org/10.1038/s41586-024-07487-w.

937 Adler, J., and Parmryd, I. (2010). Quantifying colocalization by correlation: The Pearson correlation
938 coefficient is superior to the Mander's overlap coefficient. Cytometry A *77A*, 733-742.
939 https://doi.org/10.1002/cyto.a.20896.

940 Amali, A.J., Awwad, N.H., Rana, R.K., and Patra, D. (2011). Nanoparticle assembled microcapsules
941 for application as pH and ammonia sensor. Anal. Chim. Acta *708*, 75-83.
942 https://doi.org/10.1016/j.aca.2011.10.001.

943 Barkawi, L.S., Tam, Y.-Y., Tillman, J.A., Pederson, B., Calio, J., Al-Amier, H., Emerick, M.,
944 Normanly, J., and Cohen, J.D. (2008). A high-throughput method for the quantitative analysis of

945 indole-3-acetic acid and other auxins from plant tissue. Anal Biochem. *372*, 177-188.
946 https://doi.org/10.1016/j.ab.2007.08.009.

947 Bellstaedt, J., Trenner, J., Lippmann, R., Poeschl, Y., Zhang, X., Friml, J., Quint, M., and Delker, C.
948 (2019). A Mobile Auxin Signal Connects Temperature Sensing in Cotyledons with Growth Responses
949 in Hypocotyls. Plant Physiol. *180*, 757-766. https://doi.org/10.1104/pp.18.01377.

950 Boitreaud, J., Dent, J., McPartlon, M., Meier, J., Reis, V., Rogozhnikov, A., and Wu, K. (2024). Chai-1:
951 Decoding the molecular interactions of life. bioRxiv 2024.10.10.615955.
952 https://doi.org/10.1101/2024.10.10.615955.

953 Bücherl, C.A., Bader, A., Westphal, A.H., Laptenok, S.P., and Borst, J.W. (2014). FRET-FLIM
954 applications in plant systems. Protoplasma *251*, 383-394. https://doi.org/10.1007/s00709-013-0595-7.

955 Chen, L., Tong, J., Xiao, L., Ruan, Y., Liu, J., Zeng, M., Huang, H., Wang, J.-W., and Xu, L. (2016).
956 YUCCA-mediated auxin biogenesis is required for cell fate transition occurring duringde novoroot
957 organogenesis in Arabidopsis. J. Exp. Bot. *67*, 4273-4284. https://doi.org/10.1093/jxb/erw213.

958 Clough, S.J., and Bent, A.F. (2008). Floral dip: a simplified method forAgrobacterium-mediated
959 transformation ofArabidopsis thaliana. Plant J. *16*, 735-743.
960 https://doi.org/10.1046/j.1365-313x.1998.00343.x.

961 Gao, Y., Zhang, Y., Zhang, D., Dai, X., Estelle, M., and Zhao, Y. (2015). Auxin binding protein 1
962 (ABP1) is not required for either auxin signaling or Arabidopsis development. Proc. Natl. Acad. Sci.
963 USA *112*, 2275-2280. https://doi.org/10.1073/pnas.1500365112.

964 Gomord V, D.L., Fitchette-Lainé AC, Satiat-Jeunemaitre B, Hawes C, and Faye L. (1997). The
965 C-terminal HDEL sequence is sufficient for retention of secretory proteins in the endoplasmic
966 reticulum (ER) but promotes vacuolar targeting of proteins that escape the ER. Plant J. *11*, 313-325.
967 https://doi.org/10.1046/j.1365-313x.1997.11020313.x.

968 Zuo, J., Niu, Q. and Chua, N. (2000). An estrogen receptor-based transactivator XVE mediates highly
969 inducible gene expression in transgenic plants. Plant J. *24*, 265-273.
970 https://doi.org/10.1046/j.1365-313x.2000.00868.x.

971 Kakei, Y., Yamazaki, C., Suzuki, M., Nakamura, A., Sato, A., Ishida, Y., Kikuchi, R., Higashi, S.,
972 Kokudo, Y., Ishii, T., et al. (2015). Small-molecule auxin inhibitors that target YUCCA are powerful
973 tools for studying auxin function. Plant J. *84*, 827-837. https://doi.org/10.1111/tpj.13032.

974 Kriechbaumer, V., Breeze, E., Pain, C., Tolmie, F., Frigerio, L., and Hawes, C. (2018). Arabidopsis
975 Lunapark proteins are involved in ER cisternae formation. New Phytol. *219*, 990-1004. https://doi.org/
976 10.1111/nph.15228.

977 Li, C., Yeh, F.L., Cheung, A.Y., Duan, Q., Kita, D., Liu, M.C., Maman, J., Luu, E.J., Wu, B.W., Gates,
978 L., et al. (2015). Glycosylphosphatidylinositol-anchored proteins as chaperones and co-receptors for
979 FERONIA receptor kinase signaling in Arabidopsis. Elife *4,* e06587.
980 https://doi.org/10.7554/eLife.06587.

981 Lin, W., Zhou, X., Tang, W., Takahashi, K., Pan, X., Dai, J., Ren, H., Zhu, X., Pan, S., Zheng, H., et al.
982 (2021). TMK-based cell-surface auxin signalling activates cell-wall acidification. Nature *599*, 278-282.
983 https://doi.org/10.1038/s41586-021-03976-4.

984 Liu, F., Qu, P.Y., Li, J.P., Yang, L.N., Geng, Y.J., Lu, J.Y., Zhang, Y., and Li, S. (2024). Arabidopsis
985 protein S-acyl transferases positively mediate BR signaling through S-acylation of BSK1. Proc. Natl.
986 Acad. Sci. USA *121*, e2322375121. https://doi.org/10.1073/pnas.2322375121.

Liu, Z., Chu, X., Ren, W., Cheng, L., Liu, C., Wang, C., Gao, S., Dai, S., and Li, C. (2025a). PCP-B peptides and CrRLK1L receptor kinases control pollination via pH gating of aquaporins in Arabidopsis. Dev. Cell *60*, 1336-1347. https://doi.org/10.1016/j.devcel.2024.12.026.

Shelton, V. (2025). Determining the Effectivity of PyMOL Approaches Through the Experimental Evaluation of Lactoferrin Binding.

Sun, N., Wang, J., Gao, Z., Dong, J., He, H., Terzaghi, W., Wei, N., Deng, X.W., and Chen, H. (2016). Arabidopsis SAURs are critical for differential light regulation of the development of various organs. Proc. Natl. Acad. Sci. USA *113*, 6071-6076. https://doi.org/10.1073/pnas.1604782113.

Sylvain Merlot, N.L., Francesca Fenzi, Christiane Valon, Miguel Costa, Laurie Piette, Alain Vavasseur, Bernard Genty, Karine Boivin, Axel Mu¨ ller, Je´roˆme Giraudat and Jeffrey Leung (2007). Constitutive activation of a plasma membrane Hþ-ATPase prevents abscisic acid-mediated stomatal closure. EMBO J. *26*, 3216-3226. https://doi.org/10.1038/sj.emboj.7601750.

Yang, Z., Xia, J., Hong, J., Zhang, C., Wei, H., Ying, W., Sun, C., Sun, L., Mao, Y., Gao, Y., et al. (2022). Structural insights into auxin recognition and efflux by Arabidopsis PIN1. Nature *609*, 611-615. https://doi.org/10.1038/s41586-022-05143-9.